



**HAL**  
open science

# Frictionless bead packs have macroscopic friction, but no dilatancy.

Pierre-Emmanuel Peyneau, Jean-Noël Roux

► **To cite this version:**

Pierre-Emmanuel Peyneau, Jean-Noël Roux. Frictionless bead packs have macroscopic friction, but no dilatancy.. 2008. hal-00250364v1

**HAL Id: hal-00250364**

**<https://hal.science/hal-00250364v1>**

Preprint submitted on 11 Feb 2008 (v1), last revised 3 Sep 2008 (v2)

**HAL** is a multi-disciplinary open access archive for the deposit and dissemination of scientific research documents, whether they are published or not. The documents may come from teaching and research institutions in France or abroad, or from public or private research centers.

L'archive ouverte pluridisciplinaire **HAL**, est destinée au dépôt et à la diffusion de documents scientifiques de niveau recherche, publiés ou non, émanant des établissements d'enseignement et de recherche français ou étrangers, des laboratoires publics ou privés.

# Frictionless bead packs have macroscopic friction, but no dilatancy.

Pierre-Emmanuel Peyneau\* and Jean-Noël Roux  
Université Paris-Est, LMSGC<sup>†</sup>, Institut Navier, 2 allée Kepler,  
Cité Descartes, 77420 Champs-sur-Marne, France  
(Dated: February 11, 2008)

The statement of the title is shown by numerical simulation of homogeneously sheared packings of frictionless, nearly rigid beads in the quasistatic limit. Results coincide for steady flows at constant shear rate  $\dot{\gamma}$  in the limit of small  $\dot{\gamma}$  and static approaches, in which packings are equilibrated under growing deviator stresses. The internal friction angle  $\varphi$ , equal to  $5.76 \pm 0.22$  degrees in simple shear, is independent on the average pressure  $P$  in the rigid limit. It is shown to stem from the ability of stable frictionless contact networks to form stress-induced anisotropic fabrics. No enduring strain localization is observed. Dissipation at the macroscopic level results from repeated network rearrangements, like the effective friction of a frictionless slider on a bumpy surface. Solid fraction  $\Phi$  remains equal to the random close packing value  $\simeq 0.64$  in slowly or statically sheared systems. Fluctuations of stresses and volume are observed to regress in the large system limit, and we conclude that the same friction law for simple shear applies in the large system limit if normal stress or density is externally controlled. Defining the inertia number as  $I = \dot{\gamma}\sqrt{m/(aP)}$ , with  $m$  the grain mass and  $a$  its diameter, both internal friction coefficient  $\mu^* = \tan\varphi$  and volume  $1/\Phi$  increase as powers of  $I$  in the quasistatic limit of vanishing  $I$ , in which all mechanical properties are determined by contact network geometry. The microstructure of the sheared material is characterized with a suitable parametrization of the fabric tensor and measurements of connectivity and coordination numbers associated with contacts and near neighbors.

PACS numbers: 45.70.-n, 83.80.Hj, 81.40.Lm, 83.10.Rs

## I. INTRODUCTION

Packings of particles appear in a variety of fields of condensed matter physics and material science, such as granular materials [1, 2, 3], powders [4], or concentrated, non-colloidal suspensions [5, 6]. Such systems are macroscopically disordered, on a scale such that traditional statistical mechanical approaches are irrelevant, and share many common features in their rheological behavior. One is a certain shear stress threshold, above which they roughly qualify as a fluid, and below which they might be regarded as solid. In assemblies of particles with purely repulsive force laws, interactions often do not introduce any stress scale, and the threshold only involves some *ratio* of stress components, whence a behavior often expressed as a *friction law*. Another basic property shared by many particulate systems is the existence of a specific value of the particle density, below which the material cannot flow. The viscosity of a dense suspension diverges as the solid fraction  $\Phi$  approaches some value  $\Phi^*$ , often regarded [7] as identical to the random close packing one,  $\Phi_{\text{RCP}}$  ( $\Phi_{\text{RCP}} \simeq 0.64$  for identical spherical balls [8]). Shearing and volumetric strains are coupled in granular media, which, once densely packed, cannot deform without expanding: this is the dilatancy property,

first introduced by Reynolds [9]. Once the shear strain reaches a large enough value, granular packs can continuously deform, like perfectly plastic materials, under constant stresses while keeping a constant solid fraction  $\Phi_c$ : this state of steady plastic flow does not depend on initial conditions and is known in soil mechanics as the *critical state* [10]. Friction and dilatancy are coupled in granular materials by the stress-dilatancy relations, as proposed, *e.g.* by Rowe [10, 11].

It is tempting to try and identify simple, model systems apt to explore the microscopic origin of those broadly defined rheological features. To this end, discrete particle numerical simulation, for granular materials [1, 12, 13], or suspensions [14], has now become a widespread research tool. Thus friction laws in model granular assemblies in steady shear flows, with some inertial effects, were simulated [15, 16], and stress-dilatancy relations were tested [17]. Many results were obtained on sphere packings [18, 19], which, long investigated in order to characterize their geometry [8, 20], are now studied with complete mechanical models. Thus it has been checked [21, 22, 23] that the random close packing state of monosized spheres (which is simply an equilibrium configuration of frictionless, rigid beads under a uniform isotropic pressure) is apparently uniquely defined if enduring agitation inducing traces of crystalline order is avoided in the assembling stage. The macroscopic (or internal) friction coefficients, and their relation to micromechanical parameters, including intergranular friction, have been evaluated from numerical simulations [18, 19].

Despite recent advances, some open gaps and unanswered questions can be pointed out in the literature.

---

<sup>†</sup>Laboratoire des Matériaux et des Structures du Génie Civil is a joint laboratory depending on Laboratoire Central des Ponts et Chaussées, École Nationale des Ponts et Chaussées and Centre National de la Recherche Scientifique

\*Electronic address: pierre-emmanuel.peyneau@lcpc.fr

The accurate and detailed characterization of frictionless systems under isotropic loads [21, 22], in which static equilibrium states are studied, and few parameters are introduced, contrast with the more general investigations of the behavior of granular systems with intergranular friction [17, 18, 19], which are most often carried out by dynamical methods involving inertia effects, and involve quite a few additional parameters. In those latter studies, the limit of frictionless grains is not really treated with the desirable accuracy. Yet, frictionless packings, albeit reported to exhibit singular properties [24, 25, 26], incorporate basic geometric effects that are common to suspensions and dry granular systems, even though they are supplemented by viscous flow effects in the first case, by intergranular friction and inertia in the second case.

In order to clarify issues that have not been settled, the present paper is devoted to a numerical study of *frictionless bead packings*, subjected to homogeneous shear, and addresses the following questions. Are there such things as “anisotropic random close packing states”? Can frictionless packs sustain shear stresses in static equilibrium states as well as in slow, steady flow, and do static and dynamic friction coefficients coincide? Do fluctuations on measured stresses or strain rates regress in the large system limit? What can be said about characteristic densities  $\Phi_{\text{RCP}}$ ,  $\Phi^*$ ,  $\Phi_c$ ? How do classical approaches of dilatancy [9, 27], and the way it couples to friction [17], apply in such a simple case?

The paper is organized in four main parts. Section II describes the model material and the numerical simulation setup, specifying the boundary condition and initial states used in static and dynamic approaches. Section III reports on the main results about the macroscopic behavior – macroscopic friction and dilatancy – and their dependence on the dimensionless control parameters identified in Section II. Section IV investigates the packing microstructure and the force networks, in connection with macroscopic mechanical properties, with, in particular, a detailed characterization of anisotropy. Section V is a discussion.

## II. MODEL MATERIAL AND NUMERICAL EXPERIMENTS

### A. System and interactions

We consider packings of equal-sized spherical beads of diameter  $a$  and mass  $m$ , enclosed in a cuboidal simulation cell.

Beads interact in their contacts where only normal forces  $F_N$  are transmitted, which are modeled as a sum of an elastic term and a viscous one, as in many numerical studies of granular systems (see e.g., Refs. [18, 23, 28, 29]). The elastic force  $F_N^e$  is related to the normal deflection  $h$  of the contact by the Hertz law [30],

$$F_N^e = \frac{\tilde{E}}{3} \sqrt{ah}^{3/2}, \quad (1)$$

where  $\tilde{E}$  is a notation for  $E/(1 - \nu^2)$ ,  $E$  is the Young modulus of the solid material the spherical grains are made of, and  $\nu$  its Poisson ratio. Eq. (1) attributes to contacts a variable spring constant  $K_N$ ,

$$K_N = \frac{dF_N^e}{dh} = \frac{\tilde{E}}{2} \sqrt{ah}^{1/2} = \frac{3^{1/3}}{2} \tilde{E}^{2/3} a^{1/3} (F_N^e)^{1/3}. \quad (2)$$

The viscous normal force opposes the relative normal velocity  $\delta V_N = \dot{h}$  of contacting beads, and is chosen as

$$F_N^v = \zeta \sqrt{2mK_N} \delta V_N = \zeta (m\tilde{E})^{1/2} (ah)^{1/4} \delta V_N, \quad (3)$$

with a constant coefficient  $\zeta$ . The motivation of (3) is the choice of a damping coefficient which varies in time, but stays equal to a fixed fraction  $\zeta$  of the critical damping coefficient of the harmonic oscillator defined by spring constant  $K_N$  and mass  $m/2$  (the relevant value for the relative motion in an isolated pair of interacting particles of mass  $m$ ). The same form of the viscous force was used in [23, 31]. It is admittedly devoid of a physical justification (like most models of viscous forces implemented in simulations of granular materials) and consequently the influence of parameter  $\zeta$  on the simulation results has to be carefully assessed. In practice, some kind of dissipation in relative motion of contacting particles and collisions is needed, otherwise frictionless particles would form conservative systems. One attractive feature of the force law of (3) is the resulting velocity-independent coefficient of restitution  $e_N$  in binary collisions. Most simulations reported here were done with  $\zeta$  values such that  $e_N$  is close to zero. The combination of the two normal components (1) and (3) may give rise to tensile forces between two particles in contact (an extremely rare occurrence in slow flows). We checked that this feature has no impact on the results.

Particle rotations play no role and are ignored, as frictionless spherical objects behave like point particles interacting with central forces.

The equations of motion for the particles, given by Newton’s law, as in all molecular dynamics (MD) methods, are to be numerically solved with standard time discretization schemes [32], and the procedure is similar to the ones employed in a host of recent numerical studies of granular systems (Refs. [16, 19, 23, 28, 29, 31] are but a few examples). The time step used in the computations is a small fraction of the characteristic period of oscillations in one contact, with

$$\Delta t = \delta \sqrt{\frac{m}{K_N}}, \quad \text{with } \delta \ll 1. \quad (4)$$

As  $K_N$  varies with  $h$  or  $F_N$  according to (2), the time step is chosen with reference to the typical largest elastic intergranular force, and therefore changes with the stress level in the system.

In Sec. IIB we specify how stresses or strain rates are controlled. The boundary conditions are such that the macroscopic stress identifies with the classical expression,

which applies to granular systems [33, 34], as well as to simple liquids [35], in the frame of reference of the center of mass of the whole system:

$$\underline{\underline{\sigma}} = \frac{1}{\Omega} \left[ \sum_{i=1}^N m_i \vec{v}_i \otimes \vec{v}_i + \sum_{i < j} \vec{F}_{ij} \otimes \vec{r}_{ij} \right] \quad (5)$$

We use the convention that compressive stresses are positive. In (5), the second term within brackets is a sum over all interacting pairs  $i, j$ ,  $\vec{F}_{ij}$  is the force exerted by particle  $i$  onto  $j$ , and vector  $\vec{r}_{ij}$  points from the center of  $i$  to the center of  $j$  ( $\vec{r}_{ij}$  should be defined with the nearest image convention if periodic boundary conditions are used). The first term vanishes in mechanical equilibrium.

## B. Boundary conditions, stress and strain control

We use different simulation procedures in which some strain, or strain rate, and stress components are externally imposed to the system. We first describe the different procedures in global physical terms (Secs. IIB1 to IIB3), while the computational details, with the appropriate equations and parameter values, are presented in Appendix A.

In order to avoid all wall effects and to determine more easily the intrinsic constitutive laws that apply in the large system limit, the simulation cell has periodic boundary conditions (possibly affected by the Lees-Edwards procedure for sheared systems [32]) in all three directions. The edges of the cell have lengths  $(L_\alpha)_{1 \leq \alpha \leq 3}$  along the three orthogonal axes of coordinates, and even though  $L_\alpha$ 's may vary the cell remains rectangular parallelipipedic, it does not distort or rotate.  $\Omega = L_1 L_2 L_3$  denotes its volume. Unlike the cell, the *material* undergoes some shear strain, imposed with the Lees-Edwards procedure [32], to be recalled below. Adding this possibility to the shrinking deformations along the three axes of coordinates, four independent strain components are considered in the different simulation steps and methods we are using in this work. The procedures defined below consist in choosing to fix some of them to zero or to a constant value while prescribing the values of stresses conjugate to the others. Table I recapitulates those choices for the three different simulation procedures.

### 1. Initial assembling process: procedure O

In a preliminary step, the system is first prepared by isotropic compression of a loose “gas” of particles. The corresponding procedure, denoted as “O” (like “origin”), is the one applied in [23] to prepare isotropic packings. Global shear strain  $\gamma$  is kept equal to zero, while the system shrinks along all three directions, until a mechanical equilibrium state is reached for which all three diagonal components  $\sigma_{\alpha\alpha}$  of the Cauchy stress tensor are equal

to a set pressure value  $P$ . The system is deemed equilibrated when all forces compensate to zero, with a tolerance set to  $10^{-4} P a^2$  on each particle, and each diagonal stress component, as computed with formula (5) is equal to  $P$  with a relative error smaller than  $10^{-4}$ , while the kinetic energy per particle does not exceed  $10^{-8} P a^3$ . Those isotropic equilibrated configurations are the “random close packing states”, as studied in [21, 22, 23] and they are accurately determined here to compare their internal states with those of sheared systems.

### 2. Controlled shear rate: procedure D

Initial configurations produced with method O are then subjected to a simple shear deformation, in which a macroscopic motion along direction 1 is set up, with velocity gradient, on average, along direction 2, while  $L_3$  and  $L_1$  are fixed.  $L_2$  is allowed to fluctuate in order to maintain, on average, a prescribed value  $\Sigma_{22}$  of stress  $\sigma_{22}$ . The macroscopic shear rate  $\dot{\gamma} = -\frac{\partial v_1}{\partial x_2}$  is imposed with the Lees-Edwards method: the neighboring periodic copy of the simulation cell for larger  $x_2$  values is moving with velocity  $-\dot{\gamma} L_2$  in direction 1. (Minus signs stem from our choice of a convention for strain parameters, which should be consistent with the one for stresses). Meanwhile, stress  $\sigma_{22}$  is maintained equal to  $P$  on average (with very small fluctuations). This defines procedure “D” (for dynamically sheared). One then records the time-averaged shear stress  $\tau = \langle \sigma_{12} \rangle$ , as well as the sample volume. The Lees-Edwards boundary condition for simple shear is illustrated on Fig. 1. It is important to note that it is fully compatible with either a linear velocity profile or very heterogeneous strain fields, as when shear localizes to thin bands. It was implemented in a very similar way in [36]. Note that the Lees-Edwards

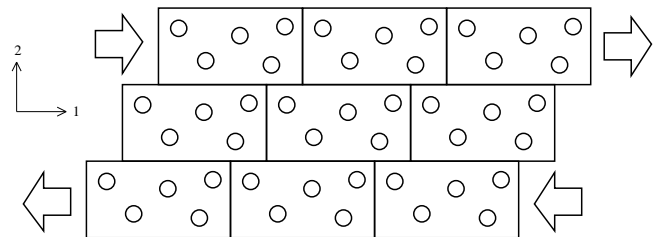


FIG. 1: Sketch of the Lees-Edwards condition imposing simple shear flow, with average velocities in direction 1 and velocity gradient parallel to direction 2. Periodic copies of any particle with different coordinates  $x_2$  are shifted along direction 1 by integer multiples of  $\gamma L_2$ ,  $\gamma$  denoting a global shear strain. With our convention,  $\dot{\gamma}$  is negative in this picture.

condition imposes a constant *shear rate*. If a *shear strain* is defined at time  $t$  as the opposite of the average displacement gradient, i.e.,  $\gamma(t) = -\Delta(t)/L_2(t)$  (the sign stems from our convention for strains and stresses),  $\Delta(t)$  denoting the offset along axis  $x_1$  of the neighbor copy of the cell in the  $x_2$  direction (see Fig. 1), then, due to

Stress/strain control	Procedure O	Procedure D	Procedure S
$\sigma_{11} / L_1$	$\sigma_{11} = P$	constant $L_1$	$\sigma_{11} = P$
$\sigma_{22} / L_2$	$\sigma_{22} = P$	$\sigma_{22} = P$	$\sigma_{22} = P$
$\sigma_{33} / L_3$	$\sigma_{33} = P$	constant $L_3$	$\sigma_{33} = P$
$\sigma_{12} / \dot{\gamma}$	$\dot{\gamma} = 0$	constant $\dot{\gamma}$	$\sigma_{12} = \tau$

TABLE I: Choice of imposed stresses or strain rates in the three simulation procedures O, D, and S.

fluctuations in length  $L_2$ , the time derivative of  $\gamma$  is not strictly equal to the constant  $\dot{\gamma}$ .

### 3. Static approach, controlled shear stress: procedure S

In the limit of small  $\dot{\gamma}$ , results of procedure D simulations should be comparable to static computations, in which the system equilibrates under an externally imposed shear stress. To compare static and dynamic measurements (possible differences between “static” and “dynamic” friction coefficients or threshold shear stresses in similar systems are mentioned in [16], and discussed in [29, 37]), we also implemented a completely stress-controlled, quasistatic procedure, denoted as “S” (for *static*). In procedure S increasing values of shear stress  $\tau$  are stepwise applied, by increments  $\delta\tau = 0.005 \times P$ , to the initially isotropic configurations obtained with procedure O, while the prescribed value of all three diagonal components  $\sigma_{\alpha\alpha}$  is the initial pressure  $P$ .  $\dot{\gamma}$ , unlike in procedure D, is not constant. It satisfies a dynamical equation, written down in Appendix A, which is designed to impose prescribed value  $\tau$  to  $\sigma_{12}$ . For each value of  $\tau$ , one waits until a satisfactory equilibrium state is reached (with the same tolerance levels as in procedure O). The calculation is stopped when the packing does not equilibrate with the current value of  $\tau$  after  $5 \times 10^7$  MD time steps. The largest  $\tau$  value for which an equilibrium state was obtained is kept as an estimate of the shear stress threshold for onset of flow, which we are going to compare to the measured average  $\sigma_{12}$  in D type simulations with small  $\dot{\gamma}$ .

### C. Dimensional analysis, state parameters and geometric limit

We are primarily interested in the macroscopic constitutive equations and the characterization of the internal states of the assembly of nearly rigid frictionless spherical grains in slow shear flow.

Consequently, we should investigate the relations between global intensive variables, such as stresses, density, strain rate, in the limit of large samples, i.e., of  $N \rightarrow +\infty$ . It is expected that for large enough samples the material state in shear flow will not depend on the specificities of boundary conditions, or on whether shear stress or strain

rate is controlled. This requires to investigate possible size effects and to study the regression of fluctuations for global variables. Measured state variables should also be uniform in space – and thus one needs to check for possible shear localization.

Assuming homogeneous steady states are observed in large enough samples, with shear rate  $\dot{\gamma}$  and normal stress  $P$ , then, by dimensional analysis [13, 15, 23] all dimensionless state variables, such as solid fraction  $\Phi$  or average stress ratio  $\langle \sigma_{12} / \sigma_{22} \rangle$  only depend on three dimensionless parameters.

The first one is the level of viscous damping  $\zeta$ , whose influence will be assessed in Sec. III.  $\zeta$  was observed to have negligible influence on steady uniform shear flows of granular materials [15].  $\zeta$ , which appears in a viscous force, should not play a major role in the quasistatic limit of very slow flow. However, it is important to keep a non-vanishing dissipation, and viscous normal forces cannot be discarded altogether.

The second parameter, the inertia number,

$$I = \dot{\gamma} \sqrt{\frac{m}{aP}} \quad (6)$$

characterizes the importance of inertial effects in dense granular flows [15, 16, 38] (for which it plays a central role in the design of successive constitutive laws [39]) or slow deformation of solid granular packings [40]. The quasistatic limit is the limit of  $I \rightarrow 0$ , which we will systematically explore. Simulations reported in the present paper were carried out with  $I$  values ranging from  $10^{-5}$  to 0.56.

Finally, the importance of contact deformation is characterized by the third dimensionless parameter, a *stiffness number* which we define, like in [23], as

$$\kappa = \left( \frac{\tilde{E}}{P} \right)^{2/3}. \quad (7)$$

$\kappa$  is such a that the typical contact deflection  $h$  under pressure  $P$  is  $\kappa^{-1}a$ . More precisely, in a packing of spherical grains under pressure  $P$ , one has, *in equilibrium*, as a straightforward consequence of Eq. (5), the exact relation [23]

$$\frac{\langle h^{3/2} \rangle^{2/3}}{a} = \left( \frac{\pi}{z\Phi} \right)^{2/3} \kappa^{-1}, \quad (8)$$

involving the *coordination number*  $z$ , i.e., the average number of force-carrying contacts per bead, which is close to 6 in frictionless bead packs under low pressure. Thus prefactor  $C$  in relation  $\langle h \rangle / a = C\kappa^{-1}$  is close to 1 in practical cases. In [23], elastic modulus  $\tilde{E}$ , in order to enable comparison of macroscopic elastic properties with experimental results [41], was attributed the suitable value for glass beads ( $E = 70$  GPa and  $\nu = 0.3$ ). Pressure levels  $P = 10$  kPa and  $P = 100$  kPa then respectively correspond to  $\kappa = \kappa_1 \simeq 39000$  and  $\kappa = \kappa_2 \simeq 8400$ . Most

$I$	$\kappa$	$\zeta$
$1 \times 10^{-5} - 0.56$	$\kappa_1 = 39000; \kappa_2 = 8400$	$0.05 - 0.98$

TABLE II: Range of dimensionless parameters used in this study.

of the present simulations of sheared samples were performed with those values of the stiffness number. In [23] these two values of  $\kappa$  were reported to be large enough for the limit of rigid grains, *i.e.*, of  $\kappa \rightarrow +\infty$ , to be approached with good accuracy in the case of static packings, while  $\kappa$  of order  $10^2$  would be too small: such low stiffness numbers induce notable changes in the properties of contact networks [40], which very likely affect the macroscopic mechanical properties under shear.

Table II sums up the values of dimensionless control parameters used in the present numerical study.

If dimensionless variables such as stress ratios or density are well behaved in the triple limit of  $N \rightarrow \infty$  (thermodynamic limit),  $I \rightarrow 0$  (quasistatic limit) and  $\kappa \rightarrow +\infty$  (rigid limit), then the observed inner states and mechanical behaviors of the packings only depend on their geometric properties – hence the name “macroscopic geometric limit” we adopted for such a situation. One of the major goals of the present study is the investigation of material properties in this limit.

Finally, as a practical application of the dimensional analysis of simulation parameters, let us note that the computational cost, expressed as a number of MD integration steps needed to reach a given shear strain  $\gamma$ , due to Eqs. (4), (7), and (8), is proportional to  $\gamma\sqrt{\kappa}/I$ .

### III. GLOBAL VARIABLES AND MACROSCOPIC BEHAVIOR

Our global observations and measurements are reported in this section. Conditions for proper observations of the intrinsic behavior of the material subjected to procedure D (shear-rate-controlled numerical experiments) are checked for in Section III A, in which various qualitative aspects of the material state in shear flow are also discussed. Attention is then focused on macroscopic friction (Sec. III B) and dilatancy (Sec. III C) properties of the material, which are more thoroughly and quantitatively investigated. Finally, the results obtained with procedure D at low inertial numbers ( $I \ll 1$ ) are compared to those of the static approach, procedure S, in Section III D. Section III E discusses the essential results and their connections with the literature on granular materials and sheared athermal particle assemblies.

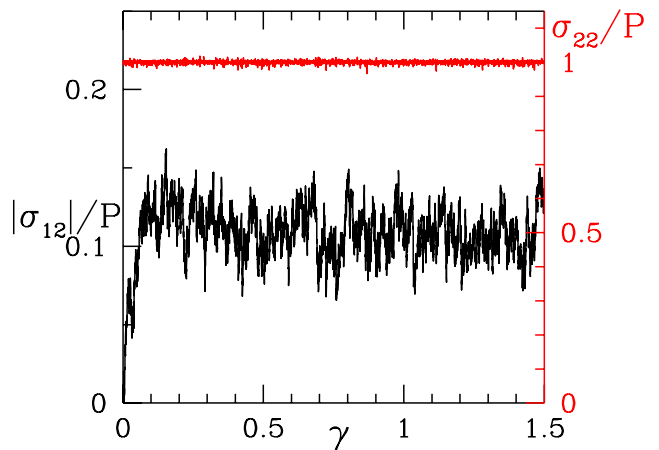


FIG. 2: (Color online)  $|\sigma_{12}|$  (left axis, in black) and  $\sigma_{22}$  (right axis, in red) as functions of strain  $\gamma$ . Note that the left and right scales are different. Time series obtained with  $I = 3.2 \times 10^{-5}$ ,  $\kappa = \kappa_1$ ,  $\zeta = 0.98$  and  $N = 4000$ .

#### A. Material state in slow shear flow: qualitative aspects

With procedure D, we investigate steady states, and time series are collected for averaging. We are interested in intrinsic constitutive laws, as measured on averaging over the whole sample. It is therefore necessary to check for both invariance in time and homogeneity, in the statistical sense. We should also assess the control of constant stress  $\sigma_{22}$ , and discuss the values of other stress components.

##### 1. Steady state flows and stress measurements

Fig. 2 displays the evolution of two components of the stress tensor,  $\sigma_{22}$  and  $\sigma_{12}$ , with strain  $\gamma$ . It shows that  $\sigma_{22}$  is well controlled since it was requested to stay equal to  $\Sigma_{22} = 0.1 P$  in this numerical experiment. The evolution of stress  $\sigma_{12}$ , from the initial, isotropically confined state, resulting from procedure O, witnesses the existence of an initial transient, which has virtually ended at  $\gamma = 0.1$  in that case. Unlike in dense systems with intergranular friction [17, 18, 19], for which deviator stresses, starting from isotropically compressed initial states, go through a peak before approaching a plateau value at large strain, the shear stress in frictionless bead packs appears to grow monotonically, as a function of strain, toward its steady state value. Another notable feature of the shear stress as a function of time is the importance of fluctuations, which often exceed 30% of the mean value on the example of Fig. 2, in a sample of 4000 beads. A proper evaluation of average shear stresses thus requires careful statistical approaches and error estimates.

As a practical criterion to detect the end of the initial transient regime, we request that a small set of ba-

sic measured quantities do not exhibit any visible trend. Specifically, shear stress  $\sigma_{12}$ , volume fraction  $\Phi$  and coordination number  $z$  should all fluctuate about their mean value in a stationary manner, as well as the kinetic energy per particle,  $\delta e_c$ , associated with velocity fluctuations. The latter is defined as

$$\delta e_c = \frac{1}{2N} \sum_{i=1}^N m_i \left[ (v_1 - \dot{\gamma} x_2)^2 + v_2^2 + v_3^2 \right] \quad (9)$$

$\delta e_c$  measures the discrepancy between the actual flow generated by the Lees-Edwards boundary condition in the granular material and the affine velocity field in a homogeneous continuum in shear flow. The steady state part of the time series starts for values of strain  $\gamma$  that depend on the inertia parameter, of order  $10^{-1}$  for the smallest  $I$  values, ( $\sim 10^{-5}$ ), increasing typically to about 0.5 for  $I = 10^{-2}$  and to several units for  $I \sim 10^{-1}$ .

Unlike  $L_2$ , lengths  $L_1$  and  $L_3$  are constrained to remain constant in procedure D, so that  $\sigma_{11}$  and  $\sigma_{33}$  may vary during the simulation. For  $I < 0.01$ , we observed that time averages of  $\sigma_{11}$  and  $\sigma_{33}$  differed from the initial hydrostatic pressure  $P$  by less than 3%. This difference becomes even smaller for smaller inertial numbers: for  $I = 10^{-3}$ , relative differences  $(\langle \sigma_{11} \rangle / P) - 1$  and  $(\langle \sigma_{33} \rangle / P) - 1$  respectively reduce to 1.0% and 2.2%. Those values decrease down to 0.9% and 1.7% for  $I = 10^{-4}$ , and to 0.6% and 1.6% for  $I = 10^{-5}$ . Although apparently not equal to zero, even in the quasistatic limit, those stress components are very small, and, consequently, will not be studied in the sequel. Sec. III B, instead, focuses on accurate determinations of shear stress  $\sigma_{12}$ .

For a given number of particles, the *relative* fluctuations of the instantaneous value of  $\sigma_{12}$ ,  $\Phi$  and  $z$  (*i.e.*, the ratio of their quadratic average to the mean value) seem to be independent of inertial number  $I$ . The average values of  $\delta e_c$ , on the other hand, as compared to the kinetic energy of the macroscopic field, which is proportional to  $\dot{\gamma}^2$ , increases as  $I$  decreases. Fig. 3 is a plot of  $\langle \delta e_c \rangle / (m a^2 \dot{\gamma}^2)$  versus inertial number, showing that this ratio approximately diverges as  $1/I$  in the limit of  $I \rightarrow 0$ . This agrees with measurements made in 2D simulations of shear flow: the same behavior is reported in Ref. [15], and an interpretation was suggested, to which we shall return in Section III E. These observations suggest that in the quasistatic limit one has increasingly inhomogeneous instantaneous velocity gradient fields, which we now investigate.

## 2. Instantaneous velocity profiles

Instantaneous velocity profiles  $v_1(x_2)$  recorded at different random times for different values of  $I$  are plotted in Fig. 4. Profiles  $v_1(x_2)$  are obtained on averaging particle velocities over slices cut alongside  $x_2$  in the simulation cell (particles contributing to several different averages if

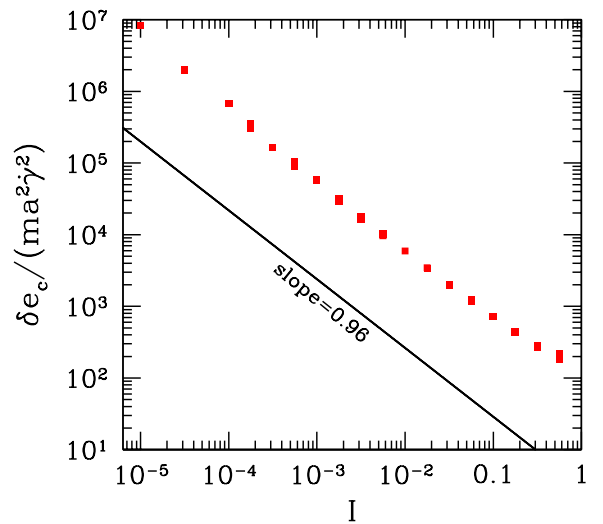


FIG. 3: Kinetic energy associated with velocity fluctuations, as defined in (9), normalized by  $m a^2 \dot{\gamma}^2$ , versus  $I$ , in simulations with 4000 beads, for  $\kappa \in \{\kappa_2, \kappa_1\}$  and  $\zeta = 0.98$ .

they overlap slice boundaries). Inertial number  $I$  has an important effect on the granular flow. As shown in Fig. 4, instantaneous velocity profiles for  $I = 3.2 \times 10^{-2}$  are linear, whereas shear bands may appear for  $I = 3.2 \times 10^{-4}$ , as in the profile marked “L” (for “localized”) on the bottom plot of Fig. 4. The transition between these two regimes seems to be gradual, with profiles in the middle part of Fig. 4, corresponding to  $I = 3.2 \times 10^{-3}$ , exhibiting somewhat intermediate features.

Localization occurs here in the bulk of the material since the system is not enclosed between walls. Localization is thus an intrinsic property of the studied material, which spontaneously appears for small values of  $I$ . Ref. [42] reports, consistently with our observations, that bulk localization appears in simulations of sheared granular materials for high enough confining pressures and/or low enough shear rates, *i.e.* for small  $I$ , near the quasistatic limit. We also believe that localization should occur more easily in soft systems since the correlation length of the strain field becomes smaller as  $\kappa$  decreases [15]. Yet, since detailed quantitative characterizations of velocity or strain fields are beyond the scope of the present study, we did not set out to chart localization tendency or intensity in the  $I$ - $\kappa$  plane.

At first glance, it seems that the erratic behavior of the velocity profiles in the quasistatic limit may seriously jeopardize the interest of the results obtained on averaging over the whole simulation size and would demand specific analyses, distinguishing between material states within and outside shear bands. However, localization patterns are not persistent, and linear velocity profiles are recovered by time averaging, even in the  $I \rightarrow 0$  limit, which means that on average, the flow is homogeneous. Figure 5 shows the gradual fading out of strain rate localization, after a strain interval of order 0.1. Shear bands

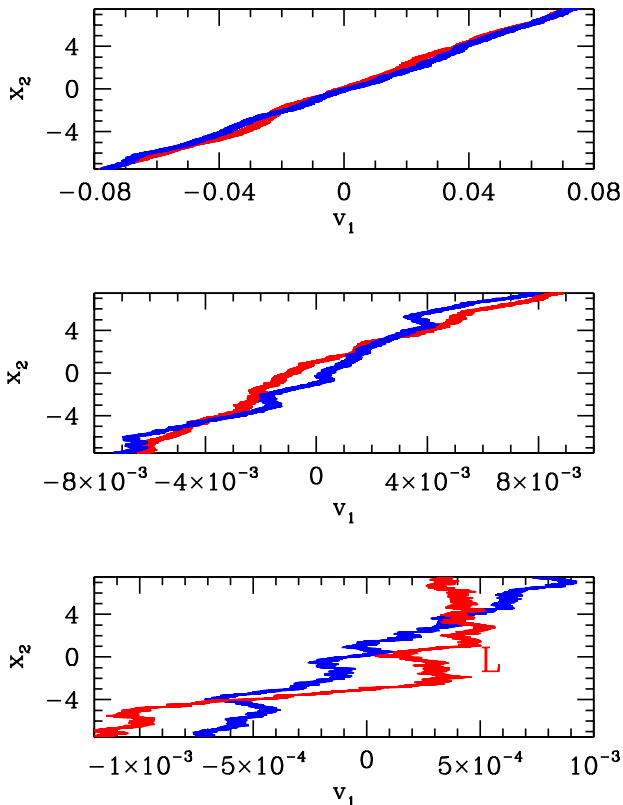


FIG. 4: (Color online) Two velocity profiles at randomly chosen times, for  $I = 3.2 \times 10^{-2}$  (top),  $I = 3.2 \times 10^{-3}$  (middle),  $I = 3.2 \times 10^{-4}$  (bottom).  $\kappa = \kappa_1$ ,  $\zeta = 0.98$  and  $N = 4000$ .

thus randomly appear, move and disappear. Such a behavior is witnessed by larger relative fluctuations of  $\delta e_c$  as  $I$  decreases. We did not carry out a detailed study of the lifetime and dynamics of nonpersistent shear bands, as the statistical homogeneity of the system in steady state shear justifies an analysis of global behavior based on averages over space and time.  $\delta e_c / (ma^2 \dot{\gamma}^2)$ , a global measure of the departure of the velocity fields from the macroscopic, affine form, smoothly increases (Fig. 3) as  $I$  decreases, but shows no sign of a different regime in the range for which temporary localized shear strains are more frequently observed.

### B. Macroscopic friction coefficient

The macroscopic friction coefficient  $\mu^*$  of the granular system is defined by analogy with the Amontons-Coulomb law commonly used in rigid body mechanics [38, 43]. For shear-rate controlled simulations (procedure D),  $\mu^*$  is set equal to the time average – in the steady state – of the ratio of the shear stress  $\sigma_{12}$  to the

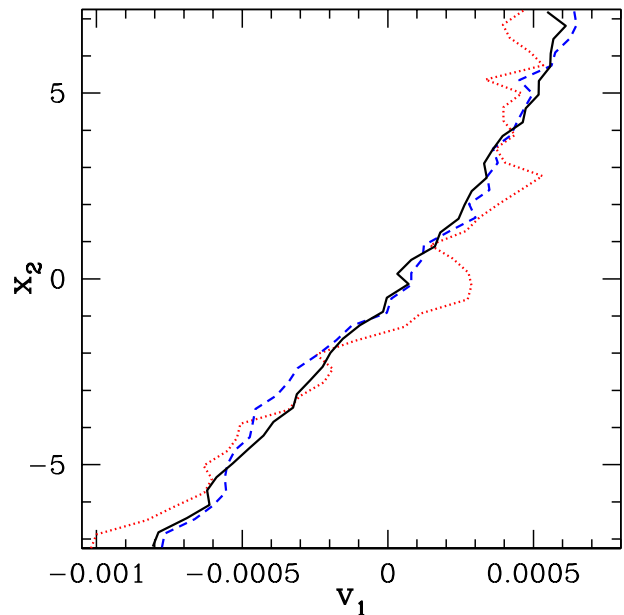


FIG. 5: (Color online) Velocity profile after shear strain intervals  $\gamma$  equal to 0.004 (red dotted curve), 0.02 (blue dashed curve) and 0.1 (black solid curve), following the instant corresponding to the localized profile marked L in Fig. 4, bottom graph.

normal stress  $\sigma_{22}$

$$\mu^* = \left\langle \frac{|\sigma_{12}|}{\sigma_{22}} \right\rangle_t \quad (10)$$

where  $\underline{\sigma}$  is the Cauchy stress tensor, defined in Eq. 5.

The shear-rate-controlled simulations performed with procedure D produce raw data in the form of time series. The steady part of the time series is isolated as explained in Sec. III A and  $\mu^*$  can then be easily computed. Note that the use of the ratio of average values in (10), instead of the average of the stress ratio, would hardly affect the measurements, since the fluctuations of  $\sigma_{22}$  (see Fig. 2) are much smaller than the fluctuations of  $\sigma_{12}$ .

To estimate the statistical uncertainty on the measurement of averages over finite time series, we use the “blocking” (or “renormalization group”) technique presented in [44]. This procedure amounts to break the whole time series, of duration  $T$ , into  $n$  subsets or “blocks” extending over smaller time intervals  $T_1 = T/n$ , evaluate averages over each one, check that the variance of the values of such averages scales as  $1/T_1$  if  $T_1$  is large enough, and then extrapolate to the complete steady state time series ( $n=1$ ). This yields error bars on measurements of averages in finite systems which should not be confused with the quadratic average of fluctuations of the observable quantity. The method identifies the minimum size of independent blocks. It does not involve any approximation and gives the correct answer when it exists provided the analyzed series is sufficiently long. In practice, due to



intrinsic long-lasting correlations in the system, we observed that quite long runs were necessary. In some cases with  $I \sim 10^{-5}$ , up to  $10^9$  simulation time steps (corresponding to a deformation  $\gamma \simeq 4$ ) were necessary for a correct evaluation of the uncertainty on  $\mu^*$ .

Continuously sheared granular materials are known to reach a shear stress plateau in steady state, at large enough  $\gamma$ , with a specific, constant inner structure – the so-called *critical state* of soil mechanics [10, 43, 45, 46]. The critical state is independent of the initial state, it is an attractor state approached by the system once the memory of the initial configuration is lost. In the present case, we could check that the time series of all observable quantities recorded in different samples were statistically identical in steady state with high accuracy.

$\mu^*$ , as estimated from time series in type D simulations, may depend on the three dimensionless numbers introduced in Sec. II C, as well as on the number  $N$  of particles. This dependence is investigated in the following paragraphs.

### 1. Effect of $I$

Among the three dimensionless parameters governing the behavior of the system, the inertial number  $I$  has the strongest effect on  $\mu^*$ . Fig. 6 plots  $\mu^*$  as a function of  $I$ . This dependence of the macroscopic friction coefficient on the inertial number is similar to the ones reported in the literature, as obtained by both simulations and experiments [15, 16, 38], although most published results pertain to granular systems with friction in the contacts. Here  $\mu^*$  approaches a finite value  $\mu_0^*$  in the quasistatic limit of  $I \rightarrow 0$ , despite the absence of friction at intergranular contacts.  $\mu_0^*$  coincides with the internal friction coefficient of the material in its critical state in the traditional sense, which implies slow enough shear rates for a quasistatic, rate independent behavior to be observed. In steady flow the power dissipated per unit volume is  $\sigma_{12}\dot{\gamma} = \mu^* P\dot{\gamma}$ . In the absence of intergranular friction the only microscopic origin of this dissipation is the viscous damping force, Eq. 3. Connections between damping and macroscopic friction are discussed below.

$\mu^*$  is an increasing function of  $I$ , starting from a finite value  $\mu_0^*$  in the quasistatic limit, i.e. when  $I \rightarrow 0$ . Note that the displayed curve is very accurate: statistical uncertainties measured with our blocking method are comprised between  $10^{-4}$  and  $10^{-3}$  and are thus invisible on the graph. We recall that the range  $I \ll 1$  is of primary interest in this work, which motivated simulations for values of  $I$  as small as  $10^{-5}$ .

### 2. Effect of $\kappa$

In the rigid limit ( $\kappa \gg 1$ ), the macroscopic behaviour should reflect the absence of stress scale in the contact law: stress ratios and derived quantities such as the

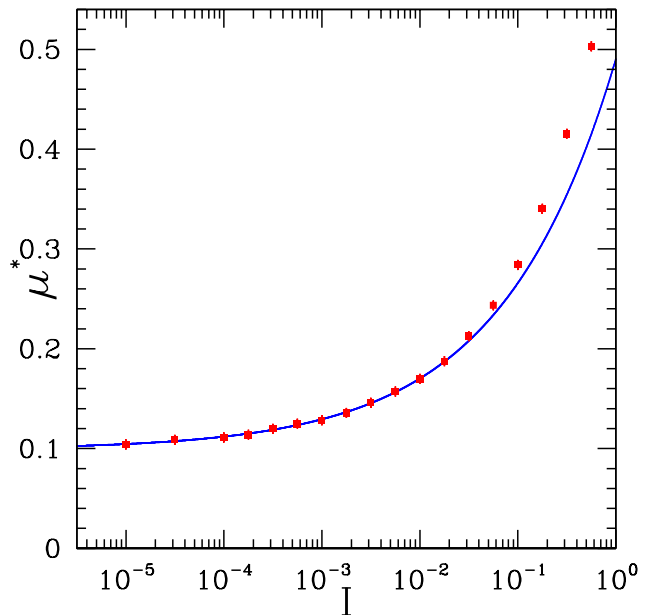


FIG. 6: Macroscopic friction  $\mu^*$  vs. inertial number  $I$  for stiffness parameter  $\kappa \in \{\kappa_2, \kappa_1\}$ , damping parameter  $\zeta = 0.98$  and number of beads  $N = 4000$ . The solid line is Eq. (12) with the parameters of Table V (no visible difference on using best parameters with  $\kappa_1$  or  $\kappa_2$ ).

macroscopic friction coefficient are expected to be independent of the average stress. As shown numerically in Tab. III, the friction coefficient hardly changes between the two values of  $\kappa$  used in our simulations, indicating that the rigid limit  $\kappa \rightarrow \infty$  is accurately approached. Those simulations were carried out with  $\zeta = 0.98$  for  $1.8 \times 10^{-4} \leq I \leq 5.6 \times 10^{-1}$ , and the relative variation on  $\mu^*$  is less than 2% throughout this range of inertia parameter on varying the stiffness parameter from  $\kappa = \kappa_1$  to  $\kappa = \kappa_2$ . However, despite the high values of  $\kappa$ , a slight systematic influence on  $\mu^*$  can still be observed. We decided nonetheless to gather the values obtained for the macroscopic friction coefficient with  $\kappa = \kappa_2$  and  $\kappa = \kappa_1$  in Fig. 6, because the uncertainty on the macroscopic, geometric limit of  $\mu^*$  to be estimated will eventually exceed this small difference.

### 3. Effect of $\zeta$

As mentioned above, the viscous damping terms are indispensable in the model, as the only source of dissipation. In the steady shear-rate-controlled simulations we are discussing, energy is continuously injected into the system and yet, the granular assembly ends up reaching a steady state, thanks to the viscous forces as defined by Eq. (3).

Consequently, the influence of the damping parameter  $\zeta$  on our results had to be assessed and we performed sim-

$I$	$\kappa$	$\mu^*$
$5.6 \times 10^{-4}$	$\kappa_1$	$0.1250 \pm 0.0006$
	$\kappa_2$	$0.1225 \pm 0.0003$
$5.6 \times 10^{-3}$	$\kappa_1$	$0.1571 \pm 0.0004$
	$\kappa_2$	$0.1554 \pm 0.0003$
$5.6 \times 10^{-2}$	$\kappa_1$	$0.2435 \pm 0.0003$
	$\kappa_2$	$0.2428 \pm 0.0002$
$5.6 \times 10^{-1}$	$\kappa_1$	$0.5031 \pm 0.0009$
	$\kappa_2$	$0.5049 \pm 0.0004$

TABLE III: Influence of  $\kappa$  on  $\mu^*$  for  $\zeta = 0.98$  and  $N = 4000$  ( $\kappa_1 \equiv 3.9 \times 10^4$ ,  $\kappa_2 \equiv 8.4 \times 10^3$ )

ulations for different values of  $I$  with  $\zeta = 0.98$  (this value corresponds to a restitution coefficient  $e_N = 3.3 \times 10^{-3}$ ),  $\zeta = 0.55$  ( $e_N = 0.17$ ),  $\zeta = 0.25$  ( $e_N = 0.49$ ) and  $\zeta = 0.05$  ( $e_N = 0.87$ ).  $\zeta$  being a dynamical parameter, its effect on  $\mu^*$  is expected to decrease as  $I$  decreases. Our results show that this is indeed the case: for  $I < 10^{-3}$ , the maximal relative variation of  $\zeta$  on the macroscopic friction  $\mu^*$  is less than 1%. Far from the quasistatic regime, the influence of  $\zeta$  is no more negligible: the relative variation of  $\mu^*$  is more than 10% on changing  $\zeta$  when  $I > 10^{-1}$ .

#### 4. Effect of $N$

The influence of the sample size on the average of the apparent friction coefficient  $|\sigma_{12}|/\sigma_{22}$ , was investigated on comparing results for three different numbers of particles:  $N = 500$ ,  $N = 1372$  and  $N = 4000$ . Results are listed in Table IV. We also recorded the standard deviations, denoted as  $\Delta\mu$ , and the average of the top percentile of the instantaneous values, denoted as  $\mu^{*,100}$ . Let us recall that we are dealing here with the fluctuations of the time series, which differ from the statistical uncertainties on the average values. As explained above, the latter can be calculated thanks to a blocking technique (the uncertainty on  $\mu^*$  displayed in Table IV lie within  $10^{-4}$  and  $10^{-3}$ ), whereas the computation of  $\Delta\mu/\mu^*$  and  $\mu^{*,100}$  are a way to evaluate the former.

The effect of the sample size on the macroscopic friction is unnoticeable for  $N = 1372$  and  $N = 4000$  since the difference between the macroscopic friction coefficients pertaining to these two sizes is less than the statistical uncertainty marring the accuracy on  $\mu^*$ . However, the impact of  $N$  on  $\mu^*$  cannot be neglected in the quasistatic limit for a system of  $N = 500$  beads. These results show that at least approximately 1000 particles are required to approach the thermodynamic limit with an acceptable accuracy.

The data of Table IV also witness the regression of fluctuations of stress ratio  $\mu^*$  in the steady state in the large system limit. The results are compatible with the classical form for the decrease of fluctuations of collective

$I$	$N$	$\mu^*$	$\Delta\mu/\mu^*$	$\mu^{*,100}$	$\Phi$	$\Delta\Phi/\Phi$	$\Phi^{,100}$
$3.2 \times 10^{-5}$	500	0.1169	0.3100	0.2188	0.6367	0.0022	0.6403
	1372	0.1101	0.1907	0.1609	0.6380	0.0015	0.6408
	4000	0.1090	0.1245	0.1431	0.6387	0.0008	0.6404
$3.2 \times 10^{-4}$	500 <sup>a</sup>	0.1432	1.263	0.8378	0.6738	0.0178	0.7148
	1372	0.1209	0.1689	0.1779	0.6365	0.0016	0.6390
	4000	0.1197	0.1002	0.1519	0.6368	0.0010	0.6388
$3.2 \times 10^{-3}$	500	0.1473	0.2091	0.2275	0.6316	0.0027	0.6360
	1372	0.1457	0.1293	0.1966	0.6322	0.0016	0.6346
	4000	0.1458	0.0764	0.1752	0.6323	0.0009	0.6338
$3.2 \times 10^{-2}$	500	0.2112	0.2045	0.3317	0.6193	0.0025	0.6234
	1372	0.2123	0.1197	0.2802	0.6197	0.0015	0.6223
	4000	0.2125	0.0694	0.2517	0.6200	0.0009	0.6215

TABLE IV: Influence of sample size  $N$  on macroscopic friction  $\mu^*$  and volume fraction  $\Phi$  for different values of inertial number  $I$ , with  $\kappa = \kappa_1$  and  $\zeta = 0.98$ . Superscripts “<sup>a</sup>” denote the average of the top percentile values in the steady state part of the time series.

<sup>a</sup>This numerical experiment displays shear-induced ordering, a feature observed only for systems of  $N < 1000$  beads (see Appendix C for details).

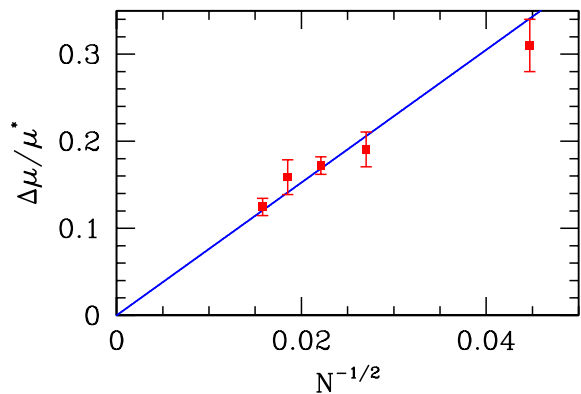


FIG. 7:  $\Delta\mu/\mu^*$  as a function of  $N$  for  $I = 3.2 \times 10^{-5}$ ,  $\kappa = \kappa_1$  and  $\zeta = 0.98$ . The solid line equation is relation (11).

variables, *viz.*  $\Delta\mu/\mu^* \propto N^{-1/2}$ . Specifically, for  $I = 3.2 \times 10^{-5}$ ,  $\kappa = \kappa_1$  and  $\zeta = 0.98$ , a fit of the data to the following form:

$$\Delta\mu/\mu^* = (7.6 \pm 0.7)N^{-1/2} \quad (11)$$

has good statistical admissibility. This result is shown in Fig. 7 in graphical form (two additional sizes  $N = 2048$  and  $N = 2916$  were also simulated). Therefore, we expect the steady state stress-strain curves such as the ones of Fig. 2, however noisy for the sample sizes simulated, to become smooth in the large system limit. The steady state in simple shear corresponds to a horizontal plateau of  $\sigma_{12}$  versus strain  $\gamma$ . This well-behaved thermodynamic

$\kappa$	$\mu_0^*$	$\alpha$	$c$
$\kappa_1$	$0.101 \pm 0.004$	$0.38 \pm 0.04$	$0.40 \pm 0.07$
$\kappa_2$	$0.100 \pm 0.003$	$0.39 \pm 0.02$	$0.42 \pm 0.03$

TABLE V: Best fit parameters for Eq. (12) and the data obtained with  $N = 4000$ ,  $\zeta = 0.98$  for  $\kappa = \kappa_1$  and  $\kappa = \kappa_2$ .

limit contrasts with the predictions of Ref [24] for the initial transient rise of shear stress as a function of strain in the quasistatic limit.

### 5. Approach to the macroscopic geometric limit

According to the previous parametric study, the macroscopic friction coefficient  $\mu^*$  depends mostly on  $I$  and is nearly independent of  $\kappa$  and  $\zeta$  for  $I \lesssim 0.01$ .  $\mu^*$  is also independent on system size provided the number of beads is sufficiently large ( $N \gtrsim 1000$  typically). Consequently, the geometric limit can be confidently studied as the limit of  $I \rightarrow 0$  on samples of 4000 beads with  $\kappa \geq \kappa_2$  and  $\zeta = 0.98$ .

$\mu^*$  should be a function of the sole inertial number in very good approximation within the range  $I \leq 0.01$ . In the absence of any scale, we tried to fit the data by a power law function (see Fig. 6) of the form

$$\mu^* = \mu_0^* + cI^\alpha \quad (12)$$

As stated above, this fit is not expected to be accurate for  $I > 0.01$ : we therefore restricted ourselves to fit the data points with  $I \leq 0.01$ , even if the curve obtained is drawn on Fig. 6 for the whole horizontal range displayed (which explains the discrepancy between the data and the fit for the largest values of  $I$ ). We neglected the very small influence of  $\zeta$ , which vanishes in the quasistatic limit, and separately estimated parameters  $\mu_0^*$ ,  $\alpha$  and  $c$  for  $\kappa = \kappa_1$  and  $\kappa = \kappa_2$  (keeping  $\zeta = 0.98$  and  $N = 4000$ ), with the results shown in Table V.

$\mu_0^*$  in (12) is the geometric macroscopic friction coefficient. Friction coefficient  $\mu^*$  corresponds to a friction angle  $\varphi$  such that  $\tan \varphi \equiv \mu^*$ :  $\varphi$  is the angle between  $\underline{\underline{\sigma}} \cdot \mathbf{e}_2$ , the stress vector on planes orthogonal to unit vector  $\mathbf{e}_2$  of the  $x_2$  axis, and  $\mathbf{e}_2$  in the simple shear test studied here. The value of the geometric macroscopic friction angle  $\varphi_0^*$  corresponding to  $\mu_0^*$  is (for  $\kappa = \kappa_1$ )

$$\varphi_0^* = 5.76^\circ \pm 0.22^\circ \quad (13)$$

Quite similar values are also reported with two-dimensional packings of polydisperse disks by Taboada *et al.* [17], whose estimate of the macroscopic friction angle lies between  $4^\circ$  and  $7^\circ$  for frictionless grains, and by Da Cruz *et al.* [15], who obtained  $\mu_0^* \simeq 0.1$  in shear flow simulations for small  $I$  parameters. Hatano [16] recently performed 3D numerical simulations on polydisperse assemblies of about 10000 spherical beads, for different intergranular friction coefficients  $\mu$ . The reported value

of the macroscopic friction coefficient in the quasistatic limit is 0.06 for  $\mu = 0$ , apparently lower than our result. It should be recalled however that Hatano's work was motivated by applications to granular materials under high confining stresses within geological fault zones, and that consequently simulations were carried out with lower stiffness levels ( $\kappa = 1840, 136, 84$  and  $42$ ) than in the present study. Moreover, the lower range of  $I$  parameters, below  $3 \times 10^{-4}$ , was only investigated with the lower  $\kappa$  values. Hatano used the same form as Eq. (12) to fit his data, but his estimate  $\alpha = 0.28 \pm 0.05$  differs from ours (see Table V). Although some effect of the polydispersity is possible, we also attribute this discrepancy to some non-negligible influence of  $\kappa$  in [16]. Only the simulations with  $\kappa = 1840$  in [16] can be expected to approach the rigid limit accurately. For this stiffness level, Hatano's data points are available for  $I \geq 3 \times 10^{-4}$  and are in very good agreement with ours (e.g.,  $\mu^* \simeq 0.17$  for  $I = 0.01$ ).

### C. Dilatancy and steady-state density

Dilatancy under shear is a basic property of granular materials in quasistatic deformation [9, 10, 11, 17], when dense samples are subjected to increasing deviator stresses. It entails that the critical value  $\Phi_c$  of the solid fraction has to be reached for steady quasistatic shear flow to be possible.  $\Phi_c$ , for a given material, is a function of  $\kappa$ . In granular flows with some non-negligible inertia effects, the material also dilates and  $\Phi$  decreases below  $\Phi_c$ . The steady-state density is mainly sensitive to parameter  $I$  if  $\kappa$  is large enough [15]. The small  $I$  behavior of frictionless bead assemblies is investigated here with greater accuracy than in previous studies. In particular we wish to clearly identify the critical volume fraction in the rigid limit in that particular case, and compare it to the random close packing value  $\Phi_{\text{RCP}}$ .

We could check that, just like the macroscopic friction coefficient, the steady state time average of the volume fraction,  $\Phi \equiv \langle \Phi(t) \rangle_t$ , is an intrinsic property of the material, independent of its initial preparation. Next, we investigate its dependence on the three dimensionless parameters  $I$ ,  $\kappa$  and  $\zeta$  and on the number of particles  $N$ .

#### 1. Effect of $I$ , $\kappa$ and $\zeta$

Once again, numerical experiments demonstrate that among the three dimensionless numbers governing the behavior of the system, the inertial number  $I$  has the most important effect on  $\Phi \equiv \langle \Phi(t) \rangle_t$ . Fig. 8 shows the influence of  $I$  on  $\Phi$ . We observe that  $\Phi$  decreases for increasing  $I$ , as previously reported [15, 16]. It starts from a value  $\Phi_0 \simeq 0.64$  in the quasistatic limit and the system expands as  $I$  increases. Statistical uncertainties on  $\Phi$  measured thanks to the blocking method are comprised between  $10^{-5}$  and  $10^{-4}$  and are thus invisible on

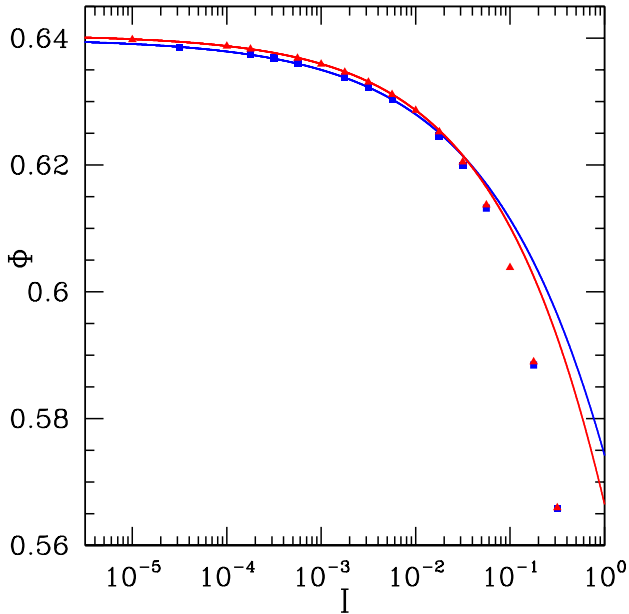


FIG. 8: (Color online) Volume fraction  $\Phi$  as a function of inertial number  $I$  (for  $\zeta = 0.98$ ,  $N = 4000$ ), for both stiffness levels  $\kappa = \kappa_1$  (blue squares) and  $\kappa = \kappa_2$  (red triangles). The solid lines are given by Eq. (17) with the parameters of Table VI.

the figure.  $\Phi_0$  is thus very close to  $\Phi_{\text{RCP}}$  [21, 23], which coincides (up to small corrections due to the finite contact stiffness) with the initial volume fraction  $\Phi^{\text{iso}}$ , right after the samples are assembled under isotropic pressure with simulation procedure O. For  $\kappa = \kappa_2$  and  $N = 4000$  we have  $\Phi^{\text{iso}} = 0.6382 \pm 0.0011$ , and  $\Phi^{\text{iso}} = 0.6369 \pm 0.0009$  for  $\kappa = \kappa_1$  (averages and standard deviations are evaluated on five samples). The system studied thus appears to be devoid of dilatancy in the quasistatic limit. Whether  $\Phi_0$  should be regarded as equal to  $\Phi^{\text{iso}} \simeq \Phi_{\text{RCP}}$  at the macroscopic level will be discussed after the possible influence of  $N$  on the average densities is investigated.

Stiffness parameter  $\kappa$  typically induces a relative increase of the volume fraction of roughly 0.1% when it changes from  $\kappa = \kappa_2$  to  $\kappa = \kappa_1$ , whatever the value of the inertial number  $I$  – a small effect, yet distinguishable from statistical uncertainties. Such a density increase is of course expected, as larger contact deflections due to larger stresses or a softer material decrease the sample volume. Simulations with  $\zeta = 0.98$  ( $e_N = 3.3 \times 10^{-3}$ ),  $\zeta = 0.55$  ( $e_N = 0.17$ ),  $\zeta = 0.25$  ( $e_N = 0.49$ ) and  $\zeta = 0.05$  ( $e_N = 0.87$ ) for a wide range of inertial numbers have also been run. The influence of  $\zeta$  on  $\Phi$  is important for large  $I$ : for  $I > 0.1$ , the relative variation of  $\Phi$  with  $\zeta$  can reach 30%. However, this effect, as expected, gradually vanishes as the quasistatic limit is approached, and for  $I < 0.01$  the relative variation of  $\Phi$  with  $\zeta$  is less than 0.1%.

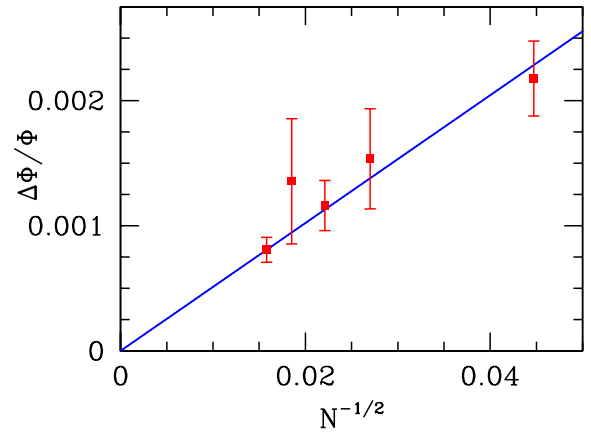


FIG. 9:  $\Delta\Phi/\Phi$  as a function of  $N$  for the same time series as in Fig. 7, fitted with Eq. (16) (solid line).

## 2. Effect of $N$

According to Table IV,  $\Phi$  very slightly varies with the number  $N$  of particles, like in static, isotropic systems [21, 23]. The following fit, based on the measurements for the smallest available value of  $I$ , i.e.,  $I = I_1 = 3.2 \times 10^{-5}$  for  $\kappa = \kappa_1$ , may be used:

$$\Phi(\kappa = \kappa_1, I = I_1, N) = \Phi_1 - k_1 N^{-1/2} \quad (14)$$

with the following parameters:

$$\begin{cases} \Phi_1 = 0.6398 \pm 0.0002 \\ k_1 = 0.070 \pm 0.008 \end{cases} \quad (15)$$

As with the macroscopic friction coefficient  $\mu^*$ , we could check for the regression of fluctuations of the volume fraction for increasing  $N$ . For the same set simulations with  $I = 3.2 \times 10^{-5}$ ,  $\kappa = \kappa_1$  and  $\zeta = 0.98$  as in Sec. III B 4, we observe that the decrease of density fluctuations with increasing  $N$  can be fitted by the following relation:

$$\frac{\Delta\Phi}{\Phi} = \frac{A}{\sqrt{N}}, \quad \text{with } A = 0.051 \pm 0.011 \quad (16)$$

as shown graphically in Fig. 9, whence a well-defined large system limit for  $\Phi$ .

## 3. Approach to the macroscopic geometric limit

Volume fraction  $\Phi$  can therefore be modelled as a function of  $I$  near the quasistatic limit, say for  $I < 0.01$ , with small corrections to account for the influence of  $N$  and  $\kappa$ . It can be regarded as independent of  $\zeta$  (at least for  $I < 0.01$ ). The fit form used is

$$\Phi^{-1} = \Phi_0^{-1} + eI^\nu \quad (17)$$

For  $N = 4000$  and  $\zeta = 0.98$ , the best fit values of the parameters of Eq. (17) are given in Table VI.

$\kappa$	$\Phi_0$	$\nu$	$e$
$\kappa_1$	$0.6398 \pm 2 \cdot 10^{-4}$	$0.39 \pm 0.01$	$0.1786 \pm 8 \cdot 10^{-4}$
$\kappa_2$	$0.6405 \pm 2 \cdot 10^{-4}$	$0.42 \pm 0.02$	$0.2038 \pm 3 \cdot 10^{-4}$

TABLE VI: Best fit parameters for Eq. (17) and the data obtained with  $N = 4000$ ,  $\zeta = 0.98$  for  $\kappa = \kappa_1$  and  $\kappa = \kappa_2$ .

To evaluate the macroscopic value  $\Phi_0^*$  in the double limit of  $I \rightarrow 0$  and  $N \rightarrow +\infty$ , it is reasonable to assume that the small corrections to  $\Phi_0^*$  that result from the finite value of  $N$  and from the nonvanishing value of  $I$  are additive. The use of Eqs. (14)-(15) to evaluate the finite  $N$  correction to the value  $\Phi_0$  of the quasistatic density, as obtained on fitting Eq. (17) to the results with  $N = 4000$ , yields, for  $\kappa = \kappa_1$ :

$$\Phi_0^* = 0.6410 \pm 0.0005 \quad (18)$$

The increases of  $\Phi$ , from its value in the rigid limit, due to the finite stiffness is of order  $\kappa^{-1}$  (an exact formula can be written down on using specific properties of packings of frictionless, rigid spheres, see [23, Eq. 31]) and is smaller than the statistical uncertainty in (18). The value of  $\Phi_0^*$  given in (18) is thus our best estimate, from D-type simulations, of the solid fraction of sheared sphere packings in the macroscopic geometric limit.

#### D. Static behavior

We now compare the results of Sections III B and III C for steady shear rate controlled simulations (procedure D) with those obtained through static shear numerical experiments (procedure S). In procedure S, all three diagonal stress components are controlled (see Table I) and stay equal to  $P$ , while  $\sigma_{11}$  and  $\sigma_{33}$  take different values in procedure D. However, as explained in Section III A, their averages are close enough to  $P$ , and their fluctuations small enough for the differences in stress states between both numerical methods to be safely neglected.

##### 1. Friction coefficient

The static macroscopic friction coefficient is defined in procedure S as

$$\mu^{\text{stat}} = \frac{|\tau_{\text{max}}|}{P} \quad (19)$$

where  $\tau_{\text{max}}$  denotes the maximum shear stress which the system has been able to sustain in mechanical equilibrium, and  $P$  the confining pressure. Static microscopic friction coefficients for different sample sizes are displayed in Table VII. Values of  $\mu^{\text{stat}}$  are larger than the dynamical value  $\mu_0^* = 0.100 \pm 0.004$  obtained in D simulations in the quasistatic limit. As shown by Tab. VII,  $\mu^{\text{stat}}$  is size

$N$	$S_N$	$\langle \mu^{\text{stat}} \rangle$	$\Delta \mu^{\text{stat}}$
256	4	0.246	0.022
500	4	0.210	0.007
1372	6	0.169	0.004
2048	6	0.154	0.004
2916	6	0.145	0.007
4000	10	0.136	0.007
8788	6	0.122	0.005

TABLE VII: Average  $\langle \mu^{\text{stat}} \rangle$  and standard deviation  $\Delta \mu^{\text{stat}}$  of the static friction coefficient obtained in S-type simulations, over  $S_N$  samples of  $N$  grains for different  $N$ . Data corresponding to both values of  $\kappa$  (with  $S_N/2$  samples each) are aggregated.

dependent, unlike  $\mu_0^*$  (for  $N \gtrsim 1000$ ). Analogous observations were reported in [29] for two-dimensional systems of frictionless disks: in the limit of vanishing shear rates, the shear stress reaches its large system limit with only several hundreds of beads, whereas the minimum shear stress required to maintain a long lasting steady shear flow exceeds the previous one and is more sensitive to  $N$ .

Fig. 10 shows the influence of system size  $N$  on  $\mu^{\text{stat}}$  (discarding the smallest  $N$  values). The data are correctly fitted by the following relation

$$\mu^{\text{stat}} = \mu_\infty^{\text{stat}} + dN^{-1/2}, \quad (20)$$

with

$$\begin{cases} \mu_\infty^{\text{stat}} = 0.091 \pm 0.009 \\ d = 2.87 \pm 0.32 \end{cases} \quad (21)$$

The related angle of friction is  $\varphi_\infty^{\text{stat}} = 5.20^\circ \pm 0.52^\circ$ . This is consistent with the equality, in the thermodynamic limit ( $N \rightarrow \infty$ ), of the dynamical and static macroscopic friction coefficients (see Eq. 13). The influence of  $\kappa$  is very small and negligible in comparison to the effect of the system size, and we therefore averaged over systems with both stiffness levels  $\kappa_1$  and  $\kappa_2$ .

With the smallest system size simulated,  $N = 256$ , we observed that some of the samples, once submitted to shear stresses, acquired a strongly ordered, crystalline structure, to be discussed in Appendix C.

##### 2. Density

Static shear simulations with procedure S support the observation made in Sec. III C that the frictionless model material studied is devoid of dilatancy in the quasistatic limit. As shown in Fig. 11, which represents  $\Phi$  as a function of the macroscopic stress ratio  $\tau/P$  imposed to the material in different samples with  $N = 4000$ , the volume fraction hardly evolves with the stress deviator as it is increased towards its maximum value. The evolution of  $\Phi$  is somewhat erratic (as in previous studies

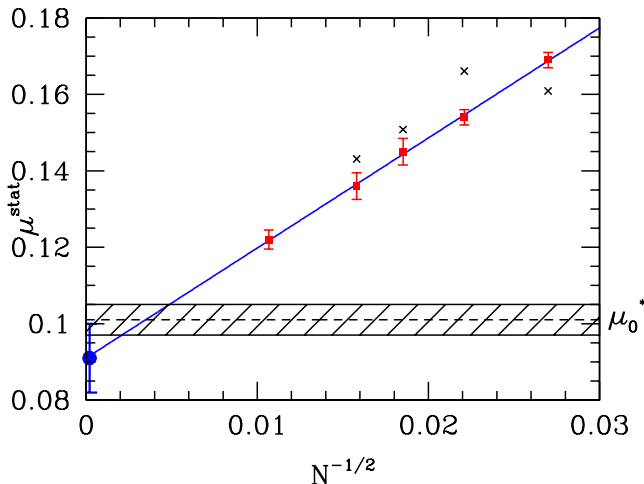


FIG. 10: (Color online) Size dependence of  $\langle \mu^{\text{stat}} \rangle$ .  $N$  denotes the number of particles in the system. The solid line is the fit of Eqs. (20)-(21). Crosses are the top percentile values extracted from the time series of  $|\sigma_{12}|/\sigma_{22}$  obtained in procedure D, as listed in Table IV. The hashed region represents the estimate, from D simulations, of  $\mu_0^*$  with its error bar (Table V). The (blue) dot with an error bar on the left axis is the static estimate,  $\mu_\infty^{\text{stat}}$ .

on 2D rigid, frictionless disk assemblies [24, 25]) and the density change between the isotropic initial state and the one supporting the maximum shear stress is equal to zero, within statistical uncertainties. Similarly to the values of  $\Phi$  measured in steady state D simulations, solid fraction  $\Phi^{\text{stat}}$  in static packings under maximum shear stress is slightly dependent on sample size, with a negative finite-size correction to the macroscopic value. On fitting a variation proportional to  $N^{-1/2}$  one gets, for  $\kappa = \kappa_1$ ,

$$\Phi^{\text{stat}} = \Phi_\infty^{\text{stat}} - k/\sqrt{N}, \quad (22)$$

with

$$\begin{cases} \Phi_\infty^{\text{stat}} = 0.6403 \pm 0.0004 \\ k = 0.125 \pm 0.026. \end{cases} \quad (23)$$

$\Phi$  values for  $\kappa = \kappa_2$  are slightly larger, by about  $10^{-3}$ .

Comparing this estimate of  $\Phi_\infty^{\text{stat}}$  with the result for  $\Phi_0^*$  given in (18), we conclude that static and dynamic solid fractions in quasistatic shear are identical, within statistical uncertainties. Disregarding the very small correction due to the finite value of  $\kappa_1$  (equal to about  $1.1 \times 10^{-4}$  on applying the formula given in [23, Eq. 31]), this means that, just like for  $\mu^*$ , the values of solid fraction  $\Phi$  in the macroscopic, geometric limit coincide in strain rate controlled and in shear stress controlled approaches.

As to the value  $\Phi^{\text{iso}}$  of the solid fraction in the initial isotropic state, a similar evaluation of size effects yields (using the samples of Table VII with  $\kappa = \kappa_1$  and  $N \geq 500$ ):

$$\Phi^{\text{iso}} = \Phi_\infty^{\text{iso}} - \frac{k_0}{\sqrt{N}}, \quad (24)$$

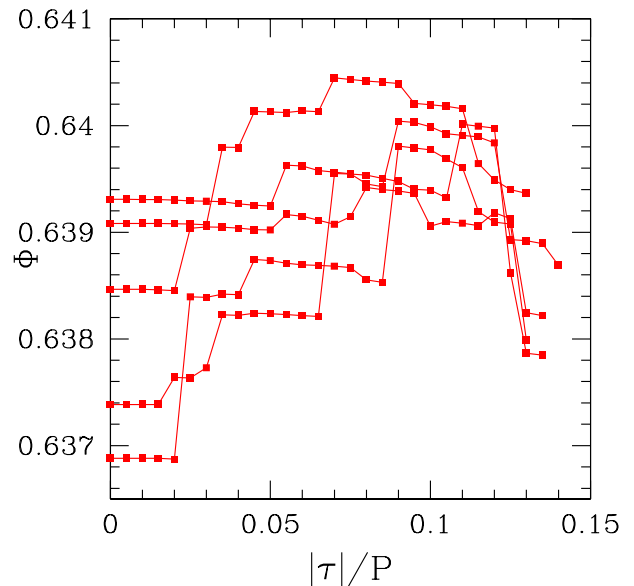


FIG. 11: Variation of the volume fraction  $\Phi$  with the static shear  $|\tau|/P$  imposed to five different samples of 4000 beads with  $\kappa = \kappa_2$ . Each curve stops at a given value of  $|\tau|/P = |\tau_{\text{max}}|/P$ : this is the greatest value for which the packing has managed to reach mechanical equilibrium.

with

$$\begin{cases} \Phi_\infty^{\text{iso}} = 0.6397 \pm 0.0008 \\ k_0 = 0.15 \pm 0.03. \end{cases} \quad (25)$$

As announced, this is the random close packing value [21, 23]. Results (25), (23) and (18) are compatible, and we thus conclude that the system is devoid of dilatancy under shear *in the macroscopic geometric limit*.

## E. Discussion

We briefly review and comment here the essential results on the macroscopic behavior of the material under simple shear, and compare them to other available results on similar systems.

### 1. Internal friction and the macroscopic geometric limit

Whether assemblies of frictionless grains have a well-defined, finite internal friction coefficient has sometimes appeared as a debatable issue, although some previously cited works [15, 16] relying on numerical simulations of slow shear flows in steady state agree with our positive conclusion. In particular, when values of  $\mu^*$  in the quasistatic critical state are studied as a function of intergranular friction coefficient  $\mu_0$ , it is sometimes assumed as obvious that  $\mu^*$  should vanish for  $\mu_0 = 0$ . Thus plots

of  $\mu^*$  as a function of  $\mu_0$  shown in Ref. [19] start at the origin of coordinates, even though no calculation with  $\mu_0 = 0$  are reported in this work. It should be emphasized that a proper evaluation of  $\mu_0^*$  in the macroscopic, geometric limit requires more care than corresponding measurements in granular assemblies with friction,  $\mu_0 > 0$ . This is due to the importance of fluctuations, as apparent on Fig. 2. In steady state dynamical simulations, it is also necessary to explore a range of very small inertial numbers to accurately evaluate the quasistatic friction coefficient, as apparent in Fig. 6 or Table III: for, e.g.,  $I = 5.6 \times 10^{-4}$ , quite a small value, the macroscopic friction coefficient already exceeds its quasistatic limit by 25%. Consequently, in the context of quasistatic simulations with variable intergranular friction  $\mu_0$ , the special case of  $\mu_0 = 0$  is seldom treated with the necessary care (although some published results are fairly compatible with ours [17, 47]).

Our estimate for  $\mu_0^*$ , the macroscopic internal friction coefficient of the material in the geometric limit, is further confirmed by the static, S-type, simulations, once their size-dependent results are suitably extrapolated to the limit of large systems. One may understand this size effect on S results as follows. The friction coefficient evaluated in D simulations is an average over time series with large fluctuations. However, the system remains close to mechanical equilibrium at any time. Assuming it is possible to find an equilibrated configuration very close to all dynamically explored states, however large the instantaneous value of the shear stress, the static S procedure would be able to find statically supported shear stress values as large as the maximum of  $\sigma_{12}$  in D time series. Although clearly oversimplifying the evolution of the system in configuration space, this explanation appears to be correct at least on correlating  $N$ -dependent maximum static shear stress levels to fluctuations in slow shear flows: the  $N$  dependence of  $\mu^{\text{stat}}$ , as plotted in Fig. 10, is paralleled by that of the typical largest values of  $\mu^*$  (top percentile) in D simulations.

Static and dynamic values of shear stress thresholds for flow are also observed to coincide in the fixed density simulation results of Xu and O'Hern [29], obtained on 2D packings of frictionless disks, with a similar excess of the static value that vanishes as  $N \rightarrow \infty$ .

When non negligible inertial effects are present, we observe that the increase of internal friction with inertial number  $I$  is the dominant feature of the material behavior (the effect of stiffness level  $\kappa$  is smaller by orders of magnitude), in qualitative agreement with many other results on frictional and frictionless grains [15, 16].

## 2. Absence of dilatancy

Our results also agree in static shear (S) and in steady state constant shear rate flows (D) for the average volume fraction  $\Phi$ , which stays equal to its value in the initial, isotropically confined configuration in the macroscopic

geometric limit. Our data show that, within statistical uncertainties (i.e., about  $5 \times 10^{-4}$ ) the critical value of  $\Phi$  is equal to  $\Phi_{\text{RCP}}$  in packings of frictionless spherical beads.

The regression of fluctuations for  $\Phi$  in the large system limit, as expressed by Eq. (16), in the constant shear rate, D procedure, implies that the state of the material in simple steady shear flow is the same for macroscopic systems, irrespective of whether density or normal stress  $\sigma_{22}$  is maintained constant.

The material studied is thus devoid of dilatancy. Interestingly, this contradicts the simple pictures of the origins of dilatancy which have been proposed since the introduction of this property by Reynolds [9], based on the distortion of simple assemblies of a small number of contacting spheres (like, e.g., a regular tetrahedron). Reynolds's ideas were discussed and generalized by Goddard and Didwania [27], who deduced estimates of the dilatancy of packings of frictionless spheres, based on statistics of Delaunay simplices obtained from numerical simulations. All such approaches predict strictly positive volume increases under shear. Sections III E 3 and IV below discuss the inadequacy of these models. Part IV also investigates the microscopic properties of such states of RCP density that support a maximum shear stress, which might be regarded as anisotropic random close packing configurations.

The absence of dilatancy in the quasistatic limit is also at odds with the classical ideas on the relation between dilatancy and internal friction, according to which macroscopic friction stems from two microscopic origins, intergranular friction and dilatancy, with an additive combination of relevant angles [11, 27] – such model systems as that of Section III E 3 providing a rationale for such a decomposition. Ref. [17] adds another component  $\varphi_0$  to macroscopic friction, due to intergranular collisions as a source of dissipation, and therefore accounts for the internal friction of frictionless grains. Thus  $\varphi_0$  is the internal friction angle that we measure in the geometric limit. Ref [17], although only incidentally dealing with frictionless materials, nevertheless appears to predict a positive dilatancy in that case, which our results do not confirm. Similarly, a recent study published by Kruyt and Rothenburg [46], which also deals with 2D disk assemblies, predicts a non-vanishing dilatancy when intergranular friction coefficient  $\mu_0$  approaches zero. Ref. [46], similarly to Ref. [17], discusses stress-dilatancy relations, and finds a linear variation of the dilatancy ratio with the difference between peak and steady-state macroscopic friction. In contradiction with our data, it attributes a positive value to both quantities as  $\mu_0 \rightarrow 0$ , while its estimate for  $\mu_0^*$  is significantly larger than our (3D) one, or than the (2D) one of Ref. [17]. (Note that the maximum deviator to mean stress ratio, as defined in [43, 46], is  $\sin \varphi \simeq \tan \varphi$ ). It seems that the case  $\mu_0 = 0$  was not directly simulated in this work, which might overlook some rapid variations of macroscopic friction and dilatancy angles with  $\mu_0$  for  $\mu_0 \ll 1$ .

In our simulations, instantaneous fluctuating shear stress and volume fraction, however, appear to be correlated, suggesting some stress-dilatancy coupling at the level of short-lived, transient and rearranging structures, which disappears on taking time averages.

### 3. A toy model

One may obtain an intuitively appealing picture of the origins of friction and dilatancy on considering a simple model in which a frictionless object slides on a bumpy surface – even though, of course, such a toy model provides a suggestive analogy, rather than a complete physical explanation of the phenomena ruling macroscopic friction and dilatancy.

The model presented here bears some similarity with the one developed in [48], and further discussed in [37], although those studies deal with a circular grain *rolling* on a bumpy surface (with an experimental realization [48]), and aim at the understanding of the avalanching behavior of a thin granular layer, rather than the bulk behavior of a homogeneous granular sample.

The mobile object has mass  $M$ , it is subject to its weight  $W$ , and it is pushed along a horizontal surface with hills and troughs. It is driven either by a constant horizontal force  $F$ , or by a piston with constant horizontal velocity  $V$ . Both contacts of the mobile object, with the piston and with the substrate, are unilateral, so that it might move faster than the piston if accelerated downhill by gravity, or even occasionally take off from the surface. A viscous force opposing the tangential motion along the surface dissipates energy, and, for  $F = 0$ , the frictionless slider stabilizes at some local elevation minimum, at the bottom of one of the depressions of the substrate.

To keep matters simple, let us consider a 2D problem with only one horizontal direction (coordinate  $x_1$ ) and a surface profile  $h(x_1)$  with alternating minima and maxima of vertical coordinate  $x_2$ , periodic with wavelength  $\lambda$  (Fig. 12). Force  $F$  is the analog of shear stress  $\sigma_{12}$  in the granular material, and  $W$  that of  $\sigma_{22}$ , while horizontal and vertical displacements respectively correspond to shear strain and vertical strain (or volume increase). Points of minimum potential energy, like point O on the figure, correspond to equilibrium states under isotropic pressure.

Let us first discuss the static experiment. The mobile object is subjected to a growing horizontal force  $F$ . Starting from O, it equilibrates where the tangent direction to the substrate is orthogonal to the applied force,  $\frac{dh}{dx} = F/W$ . Under  $F > 0$ , it had to move upwards, hence some *dilatancy*. The maximum value of  $F/W$  is the static effective friction coefficient  $\mu_S = \tan \varphi$  of the point on the surface, it is the maximum slope of profile  $h(x_1)$ , reached at point S on the figure. Effective static friction angle  $\varphi$  is the maximum angle between the reaction of the substrate, force  $\mathbf{R}$  on Fig. 12, and the vertical direction. The

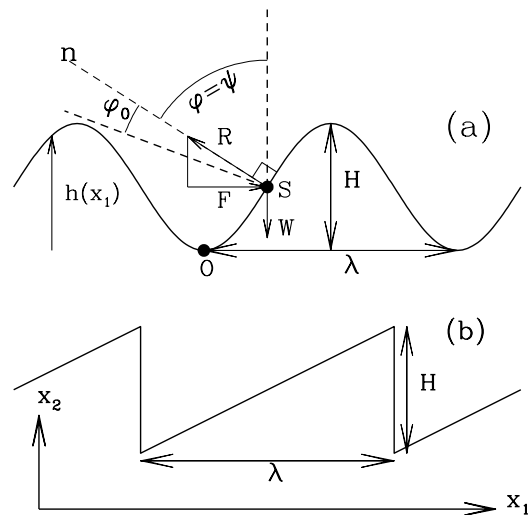


FIG. 12: The model of the slider on a rough surface. (a) Case of a sinusoidal profile. Forces at point S are drawn as vectors. (b) Profile for which  $\mu_D = \mu_S$ .

quasistatic motion from O to S follows the surface, and hence the dilatancy  $\tan \psi$  (corresponding to ratio  $\dot{\epsilon}_{22}/\dot{\gamma}$  in the sheared granular material), defined as the ratio of vertical to horizontal coordinates of the velocity, is also identical to the maximum profile slope. Dilatancy and friction angles coincide:  $\psi = \varphi$ . If a nonzero friction coefficient  $\mu_0 = \tan \varphi_0$  is introduced in the contact between the mobile object and the substrate, then reaction  $\mathbf{R}$  at point S (see Fig. 12) may form an angle  $\varphi_0$  with normal direction ( $S\mathbf{n}$ ), so that the effective static friction angle is  $\varphi = \varphi_0 + \psi$ . This coincides with some classical forms of the *stress-dilatancy relation* [10, 17], relating the macroscopic friction angle to dilatancy and microscopic, intergranular friction. In fact, stress-dilatancy relations were originally obtained with similar models: the friction of two rough surfaces onto each other can be dealt with just like the simple system we are using here, and those surfaces are granular planes in regular bead packings in Ref. [11].

In order to calculate the dynamic friction coefficient in the velocity-controlled case, it is convenient to evaluate the dissipation of energy. In the limit of small velocity, the mobile object overtakes the velocity-controlled driving piston at each maximum of  $h(x_1)$ . Its subsequent downhill sliding is accelerated by gravity, but the slider is prevented by viscous dissipation to pass the next maximum, and ends up at the bottom of the valley, where it is later picked up by the slow piston, to be pushed up the next ascending slope. In this scenario (with no take off) the dissipated energy per wavelength  $\lambda$  is the potential energy loss  $HW$  in a fall over height  $H$ . Hence an effective friction coefficient  $\mu_D = H/\lambda$ . This result is, remarkably, independent of the viscous damping coeffi-



cient, which is analogous to the behavior of the granular material in slow shear flow. Note also that the ingredients of the model are simply geometry and inertia, and that the limit of slow imposed velocity is the *geometric limit*.

The *macroscopic limit*, in this model, can be defined as  $\lambda/L \rightarrow 0$ , where  $L$  is the length scale on which the effective properties of the moving slider are studied. Consequently, the vertical motion of the sliding object, on the scale of microscopic asperities of the surface, becomes irrelevant, and one observes *effective macroscopic friction without dilatancy* – like in the granular material made of frictionless beads. Models for dilatancy [27] focus on microscopic phases of the motion in which the slider rises up the slope, but ignore the equally important ones in which it falls down.

In general, the dynamic coefficient is smaller than the static one,  $\mu_D < \mu_S$ , because  $\mu_D$  is the *average* slope of the ascending part of the profile, which is, furthermore, multiplied by the fraction of length for which  $h(x_1)$  is increasing, while  $\mu_S$  is the *maximum* slope. Thus, for a sinusoidal profile,  $h(x_1) = H/2 \sin(2\pi x_1/\lambda)$ , as represented on Fig. 12(a), one has  $\mu_S = \pi H/\lambda$ , while  $\mu_D = H/\lambda$ . In order for both friction coefficients to coincide, function  $h(x_1)$  should be as shown on Fig. 12(b), with constant slope ascending parts, followed by vertical drops.

Although such a particular profile shape as that of Fig. 12(b) is unlikely to provide a relevant model for a physical surface, it can be argued to be appropriate for the analogy with the bulk material. As long as the sliding object remains in contact with the substrate, the configuration might be an equilibrium position for some (possibly negative) value of  $F$ . In the analogy with the granular material, the contact network might balance the external load for some value of the applied stress components. The free fall of the mobile object, on the other hand, is analogous to the situation of a rearranging network, which cannot support any applied load because of the missing contacts. It has been shown, in 2D simulations of rigid, frictionless disks [24], that the material deforms in a sequence of dynamical crises during which the contact network is unable to support a macroscopic stress, and that the frequency of occurrence of such crises, in terms of macroscopic stress intervals, diverges in the large system limit. This is analogous, in the toy model, to the limit of  $\lambda \rightarrow 0$  on the one hand, and also, as stable networks are only capable to support stresses in a range which shrinks to zero, to a constant slope of the rising parts of profile  $h(x_1)$ , on the other hand.

Finally, the velocity-controlled sliding of the object on the profile shown in Fig. 12(b) also provides an interpretation of inertial number  $I$  [38], and of the behavior of the kinetic energy [15]. The motion involves two characteristic times. The first one is the duration of the rising phase, in which the object is in contact with the piston and moves with horizontal velocity  $V$ :  $\tau_1 = \lambda/V$ . The second one is the duration of the free fall:  $\tau_2 \propto \sqrt{(MH/W)}$ .

Ratio  $\tau_2/\tau_1 \propto (V/\lambda)\sqrt{(MH/W)}$ , is the analog of number  $I$ . In the analogy, distance  $H$  should be replaced by some length (a typical interstice between neighboring grains to be closed for a new contact to appear) of order  $a$ ,  $V/\lambda$  corresponds to  $\dot{\gamma}$ , while force  $W$  becomes  $Pa^2$ , which is the order of magnitude of unbalanced forces on the grains during the dynamical phases of motion. The free fall phases of the motion explain why the kinetic energy is, on average, much larger than the scale  $MV^2$  associated with the macroscopic motion. More precisely, the time average  $\delta e_c$  of the kinetic energy associated with velocity fluctuations is of order  $HW(\tau_2/\tau_1)$  (for  $\tau_2 \ll \tau_1$ ), whence

$$\frac{\delta e_c}{MV^2} \propto \frac{1}{I} \frac{H^2}{\lambda^2},$$

and the behavior shown in Fig. 3 is obtained, since  $H/\lambda$  is a constant geometric factor. (The same argument is presented in [15].)

The naive model of Fig. 12 thus shares many properties with the granular material. In both cases, the microscopic motion is a succession of arrested dynamical phases, alternating with approaches to transient equilibria. The next section investigate some microscopic aspects of the granular material in more detail.

#### IV. MICROSTRUCTURE AND FORCE NETWORKS

Our specific emphasis on the *geometric limit* of the macroscopic mechanical behavior of frictionless bead packings calls for an analysis of the geometry of sheared configurations, the first motivation of which is to explain the microscopic origins of macroscopic friction. Ultimately, a model should be sought which, unlike the analogous one of Sec. III E 3, would explicitly and quantitatively describe the mechanisms, involving instabilities and network rearrangements at the microscopic level, by which the material deforms and flows. Such goals will be only partly achieved here, since, leaving the detailed study of velocity correlations and strain mechanisms for future work, we focus on simple characterizations that are local in space and time. A secondary objective is the exploration of possible packing structures, with reference to the well characterized disordered packings of equal-sized spheres under isotropic pressure, i.e., the random close packing states [21, 22, 23]. Since one important conclusion of Section III is the equality of macroscopic internal friction angles and densities in static experiments and in the limit of very slow flow, we also check here that the various microstructural variables studied, if measured in D-type simulations, approach their values observed in S-type ones in the limit of  $I \rightarrow 0$  (at least in the large system limit).

Packing geometry is essentially controlled by steric exclusion. It is classically described with a few state variables, among which the simplest ones are scalar: the

volume fraction, the coordination number, or the network connectivity, as studied here in Section IV A below. Coordination number  $z$  is the average number of force-carrying contact (or, in other words, active exclusion constraints) per grain in the system. If  $N_c$  is the number of force-carrying contacts between the  $N$  grains, then  $z = 2N_c/N$ . The connectivity is the statistical distribution of the numbers of contact forces one grain has with its touching neighbors, i.e. the set  $(p_n)$  of probabilities for one grain to be involved in  $n$  contact forces. Thus  $z = \sum_n np_n$ .

The much-studied distribution of contact force values [49, 50] is also determined in the present case (Section IV B), and we check for effects of inertia and anisotropy.

Under stress, or influenced by the history of their assembling process, the microstructure of grain packings develops anisotropic features, which are most often characterized with the *fabric tensors*, expressing statistics on orientations of normal directions at contacts, as studied in Sec. IV C. The *critical state* of soil mechanics is characterized by stationary values of  $\Phi$ ,  $z$ , and fabric tensors, which are reached after a sufficiently large interval of monotonically growing strain in the quasistatic regime [43, 45, 51].

Connectivity and fabric might also be evaluated on the network of close neighbors (separated by a gap narrower than a prescribed distance  $h$ ). Such geometric data, related to the pair correlation function [21, 22, 23, 52] have been studied in detail in isotropic RCP configurations and are useful in attempts to determine how contacts close on deforming the system, either on increasing the level of confining stress [40, 53], in which case the response is essentially elastic [41, 53], or in plastic flow, for which contact gains and losses have to be assessed to predict fabric evolution [54]. Statistics of short distance neighbors are also important to compare numerical data to direct experimental observations of packing geometries (by such techniques as fluorescence microscopy [55] or X-ray tomography [56]), which although gaining in accuracy, are often still unable to clearly resolve the list of mechanical contacts [23] from that of close neighbor pairs.

### A. Connectivity, coordination and near neighbor correlations

For the steady shear, D-type simulations, the time average fraction  $p_n \equiv \langle p_n(t) \rangle_t$  of beads having exactly  $n$  contact neighbors is strongly affected by the inertial number  $I$  as shown in Table VIII. Fraction  $p_n$  is observed to be independent of sample size  $N$  and of the initial configuration, but it is sensitive to stiffness parameter  $\kappa$ : the fraction of grains surrounded by a great number of contact neighbors grows with  $\kappa$ . Uncertainties on fractions  $p_n$  are small (between 0.01% and 0.05%) and are not reported in Table VIII.

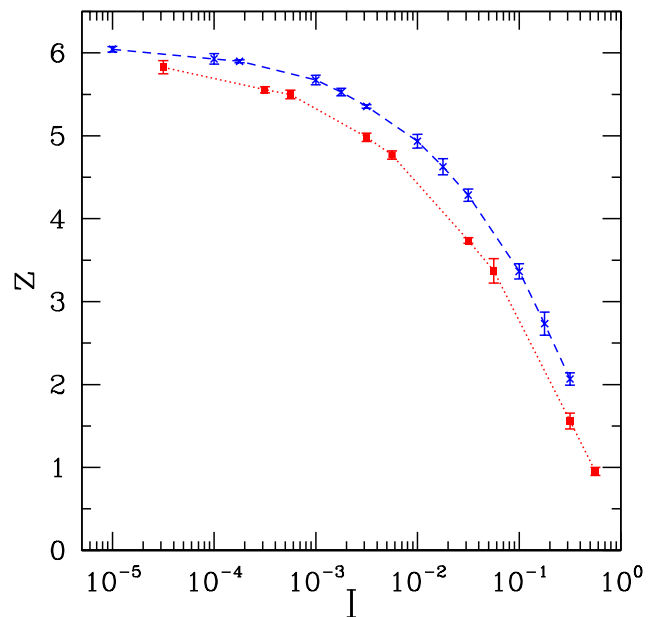


FIG. 13: (Color online) Coordination number  $z$  as a function of inertial number  $I$ , for  $\kappa = \kappa_1$  (red square dots joined by dotted line, bottom data points) and  $\kappa = \kappa_2$  (blue crosses, top, dashed line).

Distribution  $(p_n)_{n \geq 0}$  was also measured for statically sheared samples just before failure (S-type simulations). In this case,  $p_n$  is averaged over five different samples and the error on  $p_n$  is defined as the corresponding standard deviation. Results are recorded in the bottom part of Table VIII. D-type values approach those static results as  $I$  decreases, so that both connectivity distributions should coincide in the quasistatic limit. In equilibrium under static shear stress, one has  $p_1 = p_2 = p_3 = 0$ , because forces on a bead in contact with less than four other ones cannot balance, in the absence of external forces or tensile forces (thus, a 3-coordinated bead is necessarily pushed away from the plane defined by the centers of its three contacting neighbors).

Coordination number  $z = \sum_n np_n$  strongly depends on  $I$  in steady state shear flow, and it is also affected by stiffness level  $\kappa$ . It decreases with increasing inertial number  $I$ , or with increasing stiffness parameter  $\kappa$ . As to the influence of  $\zeta$  on  $z$ , it is notable for the largest  $I$  values explored, but it decreases as the quasistatic limit is approached. Larger viscous damping coefficients increase the duration of contacts in shear flow, and thus produce slightly better coordinated networks on average. However, the intensity of viscous forces becomes irrelevant in the quasistatic limit. According to our results, the  $\zeta$  dependence of  $z$  can safely be ignored for  $I < 10^{-4}$ . The  $I$  dependence of  $z$  is shown in Fig. 13.

Tab. VIII shows that the coordination number of the equilibrated (S-type) anisotropic configurations is very close to 6. This is a consequence of the isostatic-

$I$	$\kappa$	$p_0$	$p_1$	$p_2$	$p_3$	$p_4$	$p_5$	$p_6$	$p_7$	$p_8$	$p_9$	$p_{10}$
$3.2 \times 10^{-1}$	$\kappa_1$	30.0	21.8	21.8	17.9	7.40	1.1	0	0	0	0	0
$3.2 \times 10^{-2}$	$\kappa_1$	4.0	5.3	9.3	19.1	30.0	21.3	8.6	2.1	0.3	0	0
$3.2 \times 10^{-3}$	$\kappa_1$	1.6	1.4	2.2	6.7	22.1	28.4	22.3	11.2	3.4	0.5	0
$3.2 \times 10^{-4}$	$\kappa_1$	1.2	0.6	0.6	2.1	15.7	26.2	27.0	17.9	7.2	1.5	0.1
$3.2 \times 10^{-5}$	$\kappa_1$	1.2	0.2	0.2	0.6	12.6	24.1	28.3	21.1	9.4	2.2	0.2
Static (S)	$\kappa_1$	$1.3 \pm 0.2$	0	0	0	$10.8 \pm 0.4$	$22.7 \pm 0.5$	$29.1 \pm 0.8$	$23.1 \pm 0.5$	$10.2 \pm 0.5$	$2.5 \pm 0.1$	$0.3 \pm 0.1$
Static (S)	$\kappa_2$	$1.2 \pm 0.2$	0	0	0	$9.3 \pm 0.4$	$21.6 \pm 0.8$	$29.4 \pm 0.7$	$23.7 \pm 0.4$	$11.4 \pm 0.3$	$3.0 \pm 0.2$	$0.3 \pm 0.1$

TABLE VIII: Connectivity for D and S simulations.  $p_n$  denotes the percentage of particles having exactly  $n$  contacts. First five rows: data from D simulations ( $N = 1372$ ,  $\zeta = 0.98$ ). Two bottom rows: results from S simulations, averaged on five samples ( $N = 4000$ ,  $\zeta = 0.98$ ).

ity property of the force-carrying structure (also called *backbone* [23]) of equilibrated sphere packings in the rigid limit – a remarkable property discussed in several recent publications [21, 22, 23], which is specific to packings of rigid, frictionless and cohesionless spherical grains [57, 58]. The backbone comprises all  $N$  beads minus the *rattlers*, in proportion  $p_0$ , that carry no force. Isostaticity means a one-to-one correspondence between externally applied forces and normal contact forces balancing the load, or, equivalently, by duality, a one-to-one correspondence between velocities and relative normal velocities in contacts. Such mappings being linear, the spaces in correspondence have equal dimensions, and this means that the number of degrees of freedom on the backbone, i.e.,  $3N(1 - p_0)$  is equal to the number of contacts, whence a backbone coordination number, i.e.,  $z^* = z/(1 - p_0)$ , equal to 6. The data of Table VIII correspond to  $z^* \simeq 6.08$  for  $\kappa = \kappa_1$  and to  $z^* \simeq 6.16$  for  $\kappa = \kappa_2$ , witnessing the approach to the isostatic, rigid limit.

The dependence of  $(p_n)_{n \geq 0}$  on  $\kappa$  is much weaker than the dependence on  $I$  in the range explored. In faster flows, rigid clusters of connected grains have to break apart more often, contacts are lost and form looser structures of lower density (Fig. 8), as observed and discussed in the 2D numerical study of Ref. [15]. We confirm that  $I$  is really the essential state parameter ruling the transition, as it increases, between dense and collisional flows: under growing  $I$  the well connected contact network with force chains, characteristic of solid granular materials, is gradually lost and replaced by scarce, strong binary interactions. (Some early results on simulations of shear flow, as in [59], showing an effect of pressure increase on contact networks in shear flows with given shear rate  $\dot{\gamma}$ , should be interpreted as showing the influence of  $I$ , which is proportional to  $1/\sqrt{P}$ , rather than the influence of  $\kappa$ ).

Table VIII and Fig. 13 show that very low values of inertia parameter  $I$  have to be reached in order to approach the quasistatic limit with good accuracy, thus confirming the observations made for global characteristics  $\mu^*$  and  $\Phi$  in Section III. With quite low values of  $I$ , many contacts are lost ( $z$  is down to about 5 for  $I$  in the  $10^{-3}$

range). It has been often observed (see, e.g., the pictures of force patterns shown in many publications on 2D simulations [31, 60, 61]) that the grains only have a small number of contacts bearing large forces – this is the very reason why the “force chains” exist. Consequently, as contacts carrying smaller forces are necessarily shorter lived, and tend to rarefy as  $I$  increases, the populations of grains with the largest local coordination are quickly depleted –  $p_n$  is quickly decreasing at growing  $I$  for  $n \geq 7$  in Table VIII. This dependence on  $I$  is to be compared to the one of the force distribution reported in Section IV B.

If we now replace the contact network by network  $\mathcal{C}_h$  defined on declaring a bond to join all pairs of grains separated by a distance smaller than  $h$ , then its coordination number  $z(h)$  is drawn as a function of  $h/a$  in Fig. 14. In the X-ray microtomography experiments of Ref. [56], only the range  $h/a > 0.04$  would be accessible [23].  $z(h)$  starts from coordination number  $z$  at  $h = 0$  and is the cumulated integral of the pair correlation function up to distance  $a + h$  between sphere centers. The inset of Fig. 14 shows that the curves obtained with procedure D tend to merge, as the quasistatic limit is approached, with the one pertaining to S-type samples. One gets  $z(h) - z(0) \propto (h/a)^{0.6}$  for  $h/a \ll 1$  with static packings. A similar power law with exponent 0.6 has already been observed to fit  $z(h)$  data in the same range of gap  $h$  with isotropic granular packings in [22, 23]. Orientation-averaged near neighbor pair correlations are not affected by stress anisotropy in frictionless bead packs.

## B. Distribution of forces

Fig. 15 is a plot of the probability distribution function of the intergranular force normalized by the average force, for different values of inertial number  $I$ . The force distribution strongly depends on  $I$ : for  $I > 3.2 \times 10^{-2}$  the probability distribution function  $p(f)$  ( $f$  denoting the ratio of the normal force to the average value  $\langle F_N \rangle$ ) is monotonically decreasing. For smaller values of  $I$ ,  $p(f)$  has a maximum, around  $f = 0.5$ , and an approximately exponential decay for large values, as of-

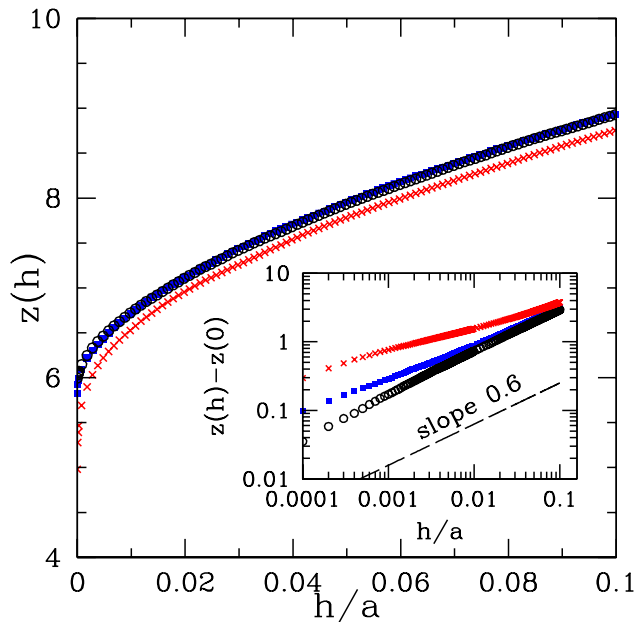


FIG. 14: (Color online) Coordination number  $z(h)$  of network  $C_h$  as a function of  $h/a$ , for  $I = 3.2 \times 10^{-3}$  (red crosses),  $I = 3.2 \times 10^{-5}$  (blue squares) and for an S-type, maximum stress deviator equilibrated configuration (black circles), with  $\kappa = \kappa_1$ . The difference between D-procedure,  $I = 3.2 \times 10^{-5}$  and static data, invisible on a linear scale, is revealed by the doubly logarithmic plot of  $z(h) - z(0)$  vs.  $h$  shown as inset.

ten observed observed in equilibrated granular packings [22, 23, 49, 50, 60, 62, 63]. The distributions obtained for the low values of  $I$  in D-type simulations gradually approach the one obtained in S-type, equilibrated packings under maximum shear stress. The Kolmogorov-Smirnov test [64] can be used to detect the influence of parameters on the force distribution – the answer depending of course on the level of statistics of the available data. Based on 10 independent configurations of 4000 grains, it leads to the conclusions that no significant difference in force distribution could be detected between S-type results under maximum shear stress and D-type ones, and no influence of  $\kappa$  either, provided the inertia parameter is small enough:  $I < 5 \times 10^{-3}$ , while some influence of  $\zeta$  is only visible for  $I > 0.1$ .

The isotaticity property of frictionless force networks in the rigid, quasistatic limit, as recalled in Section IV A, entails that force distributions are determined by the sole geometry, and do not depend on the particular form of particle interaction, which might be elastic, as in Refs. [21, 23, 28], purely viscous, as in Refs. [60, 65], or collisional, as in Refs. [22, 66]. It is interesting to investigate whether such a basic geometric property of sphere packings might depend on anisotropy. The present results, based on 10 configurations of 4000 beads, show that the difference, if it exists, is below the available statistical accuracy. Our results are compatible with a unique distribution, valid for maximum shear stress equilibrium

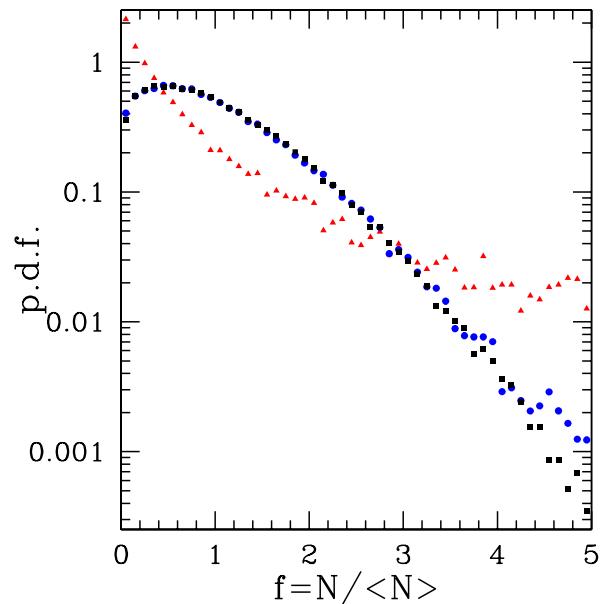


FIG. 15: (Color online) Probability distribution function of  $f = N/\langle N \rangle$  for  $I = 3.2 \cdot 10^{-1}$  (red triangles),  $I = 3.2 \cdot 10^{-3}$  (blue round dots) and  $I = 3.2 \cdot 10^{-5}$  (black square dots).

configurations as well as for isotropic ones.

### C. Fabric

Macroscopic friction is known to stem (at least partially) from the build-up of fabric anisotropy in materials made of frictional beads or disks [43, 51]. We explore this connection here, with frictionless beads.

#### 1. Anisotropy of the contact network

Anisotropy of the tridimensional contact network can be characterized by the probability density function  $E(\theta, \varphi)$  of finding a contact with direction  $(\theta, \varphi)$ .  $\theta$  is the colatitude angle, and the axis of coordinate  $x_3$ , which is parallel to the vorticity vector in the macroscopic shear flow, corresponds to  $\theta = 0$  or  $\theta = \pi$ . And  $\varphi$  is the longitude angle of the spherical coordinates, with  $\varphi = 0$  for the axis of coordinate  $x_1$ , which is parallel to the macroscopic velocity field. Numerically,  $E$  can be computed as:

$$E(\theta, \varphi) = \frac{dP}{d\Omega} \quad (26)$$

where  $d\Omega$  is the elementary solid angle and  $dP$  the fraction of contacts oriented within  $d\Omega$ .  $E$  is defined on the unit sphere of  $\mathbb{R}^3$  and thus can be expanded in a series of spherical harmonics. The coefficients of the expansion are in one-to-one correspondence with the values of the

fabric tensors, which are defined as the moments of the distribution of normal unit vectors  $\vec{n}$  on the unit sphere. Since a contact is left invariant by the parity symmetry  $\vec{r} \rightarrow -\vec{r}$ , distribution  $E$  satisfies  $E(\theta, \Phi) = E(\pi - \theta, \varphi + \pi)$ . This means that the coefficients of odd order in the expansion in spherical harmonics are all equal to zero, and corresponds to the vanishing of all odd order fabric tensors. The distribution is characterized by the series of even order ones, *viz.*

$$\langle \bigotimes_{i=1}^{2k} \vec{n} \rangle \equiv \frac{1}{N_c} \sum_{c \in \mathcal{C}} \bigotimes_{i=1}^{2k} \vec{n}_c \quad (27)$$

$\mathcal{C}$  denoting the set of  $N_c$  contacts, labelled with index  $c \in \mathcal{C}$ , where the normal unit vector is  $\vec{n}_c$ .

Keeping only the lowest order of anisotropy, the expansion of  $E$  is restricted to the spherical harmonics of order two. The coefficients (see Appendix B) are then directly related to the value of the fabric tensor of order two, denoted  $\underline{\mathbf{F}}$ :

$$\begin{aligned} E(\theta, \varphi) = & 1/(4\pi) + F_{12}d_{xy}(\theta, \varphi) \\ & + (F_{11} - F_{22})d_{x^2-y^2}(\theta, \varphi) \\ & + (F_{33} - 1/3)d_{z^2}(\theta, \varphi) + F_{13}d_{xz}(\theta, \varphi) \\ & + F_{23}d_{yz}(\theta, \varphi) + \text{higher order terms} \quad (28) \end{aligned}$$

The constant  $1/(4\pi)$  corresponds to an isotropic distribution and the next five terms of the development characterize the anisotropy of the material at the lowest order. Functions  $d$  are combinations of spherical harmonics of order two, with expressions given in Appendix B.

Fabric tensor  $\underline{\mathbf{F}}$  is computed as a time average in the steady shear simulations. Numerical experiments show that  $F_{13}$  and  $F_{23}$  are always less than their respective statistical uncertainties, and thus we can consider that these coefficients are equal to zero, as requested by the symmetry in simple shear. We observe that coefficient  $F_{12}$  is always greater (by at least one order of magnitude) than the two other nonzero anisotropic coefficients,  $F_{11} - F_{22}$  and  $F_{33} - 1/3$ . These two latter terms, as shown on Fig. 16, are below  $2 \times 10^{-3}$  for  $I < 10^{-3}$ . Such low values are comparable with sample to sample fluctuations in equilibrated configurations. Thus, in the quasistatic limit, the anisotropy can be characterized by the sole  $F_{12}$  coefficient, the limit of which, as  $I \rightarrow 0$ , is evaluated as  $F_{12}^0 = -0.0165 \pm 7 \cdot 10^{-4}$  for  $\kappa = \kappa_1$  and  $F_{12}^0 = -0.0156 \pm 7 \cdot 10^{-4}$  for  $\kappa = \kappa_2$ , with a fitting procedure. Like macroscopic friction coefficient  $\mu^*$  and solid fraction  $\Phi$ ,  $F_{12}$  strongly varies  $I$  (Fig. 16), and its dependence on  $I$  can be represented by a power law, with exponent  $\simeq 0.36$ . Fabric coefficient  $F_{12}$  slightly increases with stiffness number  $\kappa$ , as shown by Table IX.

$F_{12}$  values measured in S-type equilibrated samples under maximum shear stress are influenced by system size  $N$ , very similarly to the static friction coefficient: larger values of  $|F_{12}|$  are observed (typically  $\simeq 0.02$  for  $N = 4000$ ), but the excess over  $F_{12}^0$ , the estimate from D-type simulations in the quasistatic limit, regresses as

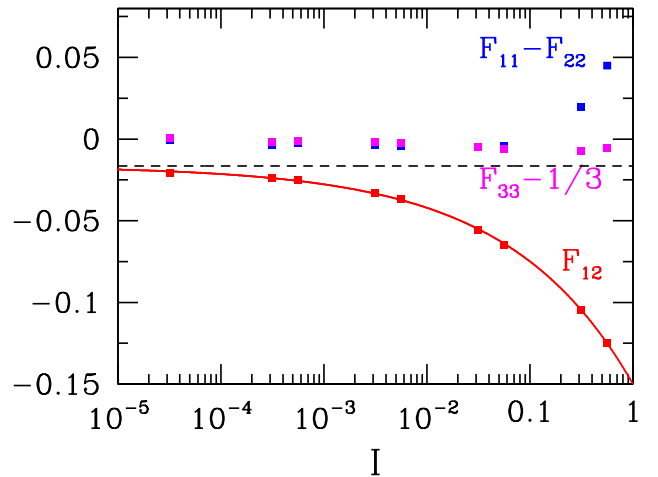


FIG. 16: (Color online)  $F_{12}$  (red),  $F_{11} - F_{22}$  (blue) and  $F_{33} - 1/3$  (magenta) as functions of inertial number  $I$ , with  $\kappa = \kappa_1$ ,  $\zeta = 0.98$  and  $N = 4000$ . The continuous line is a fit to a power law increase of  $|F_{12}|$  above some finite limit  $F_{12}^0$  for  $I \rightarrow 0$ , the value of which is indicated with the dashed horizontal line.

$I$	$\kappa$	$ F_{12} $
$5.6 \times 10^{-4}$	$\kappa_1$	0.0248883
	$\kappa_2$	0.0229216
$5.6 \times 10^{-3}$	$\kappa_1$	0.0368044
	$\kappa_2$	0.0333569
$5.6 \times 10^{-2}$	$\kappa_1$	0.0648169
	$\kappa_2$	0.0594749
$5.6 \times 10^{-1}$	$\kappa_1$	0.125109
	$\kappa_2$	0.11695

TABLE IX: Influence of  $\kappa$  on  $|F_{12}|$  for  $\zeta = 0.98$  and  $N = 4000$  ( $F_{12}$  is negative for all parameter values).

$N$  increases, and the extrapolated macroscopic limit is compatible with the estimated values of  $F_{12}^0$ . This will be further examined in the more general context of the relationship between stress and fabric anisotropies, for arbitrary stress values, in a forthcoming publication [67].

On changing  $\zeta$  from 0.98 down to 0.05,  $|F_{12}|$  increases (correlatively with the decrease of  $z$ ), by about 30% for  $I \sim 10^{-2}$ . This relative change is reduced to about 1% for  $I \sim 10^{-4}$  and the effect of  $\zeta$  vanishes in the limit of  $I \rightarrow 0$ .

Variations of fabric coefficient  $F_{12}$  with parameters  $I$ ,  $\kappa$  and  $\zeta$  are qualitatively understood on noting that  $F_{12}$  is negatively correlated with the coordination number. If there are more contacting neighbors, on average, around a sphere, they are prevented by steric constraints from achieving highly anisotropic orientation distributions. This argument, which with simple assumptions was made quantitative in 2D in Ref. [51], thus explains that the increase of  $z$  observed as  $\kappa$  is lowered tends to

reduce  $|F_{12}|$ . Similarly, the larger anisotropies observed away from the quasistatic limit are made possible by the smaller number of contacts. The increase of  $|F_{12}|$  with  $I$  is also due to the correlation of force intensities with contact directions: on evaluating separately the fabric of the subnetworks corresponding to forces larger (or smaller) than the average contact force, one typically obtains, for  $I \sim 10^{-5}$ , values of  $|F_{12}|$  twice as large (respectively: four times as small) as with the complete contact network. Contacts with small forces open if  $I$  is increased, and the remaining more strongly loaded ones are consequently more anisotropically oriented.

## 2. Connection between fabric and stress anisotropies

We now relate fabric anisotropy and shear stress. Neglecting the velocity dependent term of Eq. 5 in the quasistatic limit, one may write, with nearly rigid spheres of equal diameter  $a$

$$\begin{aligned} \underline{\underline{\sigma}} &= \frac{1}{\Omega} \sum_{1 \leq i < j \leq N} \vec{F}_{ij} \otimes \vec{r}_{ij} \\ &= \frac{N_c}{\Omega} \langle \vec{F} \otimes \vec{r} \rangle \\ &= \frac{N_c a}{\Omega} \langle F_N \vec{n} \otimes \vec{n} \rangle. \end{aligned}$$

If correlations between contact orientation  $\vec{n}$  and force values are neglected, one may replace  $\langle F_N \vec{n} \otimes \vec{n} \rangle$  by the product of averages, hence an expression of stress with the second-order fabric tensor:

$$\underline{\underline{\sigma}} = \frac{a N_c \langle F_N \rangle}{\Omega} \langle \vec{n} \otimes \vec{n} \rangle, \quad (29)$$

and the following relation for macroscopic friction coefficient  $\mu^*$ :

$$\mu^* \simeq \frac{|F_{12}|}{F_{22}} \simeq 3|F_{12}|, \quad (30)$$

since  $F_{22} \simeq 0.33$ , whatever the value of  $I$ . In the quasistatic limit, with  $F_{12} \simeq -0.017$  and  $\mu^* \simeq 0.1$ , it may be concluded that geometry accounts for roughly 50% of the macroscopic friction for our model material. This fraction of macroscopic friction explained by the sole geometry of the packing increases with increasing  $I$ . In general, the connection between macroscopic friction and fabric is influenced by many parameters, such as particle shape [68].

The missing contribution to the macroscopic friction stems from the correlation between force intensities and contact orientations. As mentioned in the end of Section IV C 1, the anisotropy of the subnetwork carrying larger than average forces is more pronounced, and such an angular dependence of force intensities increases the shear stress.

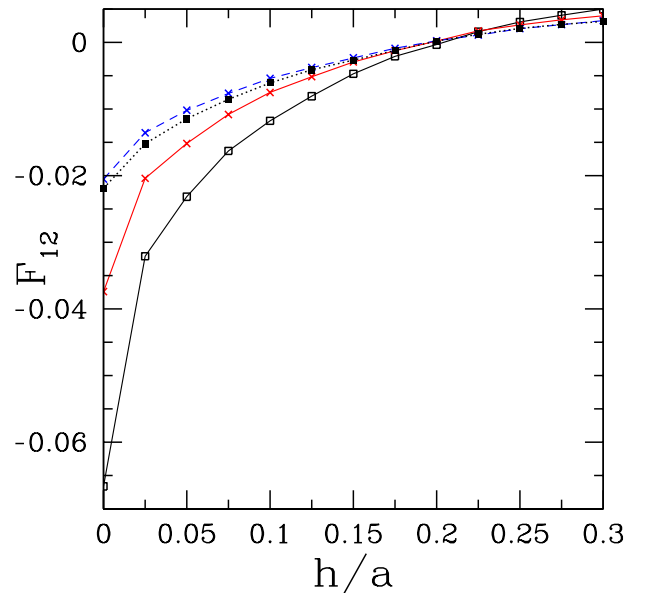


FIG. 17: (Color online) Evolution of the second-rank fabric tensor coefficient  $F_{12}$  as a function of  $h$  for  $\kappa = \kappa_2$ . Static shear simulation (black solid squares, dotted line) and four steady shear simulations:  $I = 0.1$  (black open squares, solid line),  $I = 0.01$  (red crosses symbols, solid line) and  $I = 0.0001$  (blue crosses symbols, dashed line).

## 3. $h$ -gap anisotropy

We now consider the fabric tensor of the  $h$ -network,  $\mathcal{C}_h$ . Similar relations to those written in Sec. IV C 1 hold when the contact network is replaced by  $\mathcal{C}_h$ : one can define an  $h$ -gap distribution function  $E^h(\theta, \varphi)$ , an  $h$ -gap fabric tensor ( $\langle \otimes_{i=1}^{2k} \vec{n} \rangle_h$ ), where  $\langle \cdot \rangle_h$  denotes the average on  $\mathcal{C}_h$ , and write an equation analogous to Eq. 28 for  $E^h$  and  $\underline{\underline{F}}^h$ .

The variation of  $F_{12}^h$  with  $h > 0$  is plotted in Fig. 17, with  $I$ -dependent D-results approaching S ones in the limit of  $I \rightarrow 0$ . Fig. 17 demonstrates that anisotropy (that is the absolute value of  $F_{12}^h$ ) diminishes until  $h/a \sim 0.20$  and then appears to increase by a small amount. Current cutting-edge experimental techniques like X-ray tomography would be able to detect the type of anisotropy we found in frictionless, equilibrated packings.

## V. DISCUSSION

This work was devoted to the study of frictionless identical spherical balls subjected to simple shear. The influence of the three dimensionless quantities controlling the problem – inertial number  $I$ , stiffness number  $\kappa$  and level of viscous damping  $\zeta$  – was carefully assessed and we observed that the inertial number  $I$  has the most dramatic

impact on the system behavior. Fluctuations of the measured quantities were shown to vanish for large systems. Consequently, the particular nature of the boundary conditions employed has no importance: for sufficiently large systems, fixed-volume simulations would lead to the very results we obtained with our stress driven numerical experiments. Particular attention was paid to the macroscopic geometric limit, that is the triple limit  $N \rightarrow +\infty$ ,  $I \rightarrow 0$  and  $\kappa \rightarrow +\infty$ . In this régime, the system behavior is governed by a succession of instabilities due to dynamical rearrangements of the contact network. A thorough investigation of such events remains an interesting, yet challenging, perspective.

The existence of a nonzero macroscopic friction angle was evidenced by two different kinds of simulations – shear-rate controlled dynamic calculations (D-type simulations) and quasistatic stress-controlled calculations (S-type simulations). Whereas the dynamic friction angle  $\varphi_D$  is independent of the system size for  $N > 1000$ , the static friction angle  $\varphi_S$  is very sensitive to the number of grains and is systematically greater than  $\varphi_D$  for all the studied sizes ( $N \leq 8788$ ) and  $\varphi_S - \varphi_D$  increases for decreasing  $N$ . This might be the reason why localization seems to occur more easily as the system size decreases. In finite-size systems, the shear stress is a multivaluated function of the strain rate in the quasistatic limit and the range of multivaluation increases with decreasing  $N$ . Thus shear bands are more likely to appear in small systems [15, 69, 70]. However, in the macroscopic geometric limit, we found that both friction angles  $\varphi_S$  and  $\varphi_D$  are equal within statistical uncertainties. In frictionless granular assemblies, all dissipation is due to viscous terms in contact forces, which therefore can be regarded [17] as the physical origin of macroscopic friction. However, the value of the damping coefficient  $\zeta$  is irrelevant in the quasistatic limit since the amount of dissipated energy is geometrically determined. We thus rather attribute the macroscopic friction angle to the shear-induced anisotropy of the contact network. The result that  $\varphi_S = \varphi_D$  contrasts with observations on Lennard-Jones glasses at temperature  $T > 0$  [69, 70] and on granular avalanches [71, 72]. Glass simulations show that the dynamic angle is less than the static one. This difference is linked to a stress overshoot visible on strain-stress curves. Similarly, in dense granular materials with friction, the shear stress goes through a maximum before the steady state (“critical state”) is reached, a feature which is absent in frictionless granular assemblies (both states coincide in this case). Similar differences ( $\varphi_S > \varphi_D$ ) are reported for granular flows down inclined plane. Thus, in Refs. [71, 72],  $\theta_{\text{stop}}(h)$  is less than  $\theta_{\text{start}}(h)$ , where  $\theta$  is the inclination of the plane and  $h$  the thickness of the flowing layer in the stationary state. The small thickness of the layer (typically less than ten grain diameters) and the intergranular friction are certainly responsible for this hysteresis.

The interplay between stress and dilatancy is a well known feature of granular materials. However, our sim-

ulations show that homogeneously sheared frictionless bead assemblies do not display any dilatancy in the macroscopic geometric limit. In this limit, volume fraction  $\Phi$  remains equal to  $\Phi_{\text{RCP}}$  during the whole time the material is sheared and the backbone stays isostatic in the rigid and quasistatic limits. Thus, equilibrated configurations under nonzero shear stress can be regarded as anisotropic random close packing states. This surprising lack of dilatancy has been accounted for with the help of a simple model presented in Sec. III E 3. We thus conclude that the steady state (critical) volume fraction  $\Phi_c$  is equal to  $\Phi_{\text{RCP}}$ .

The behavior of frictionless granular assemblies under arbitrary load directions will be the subject of a future work [67] in order to gain a better knowledge of the yield surface and of the mechanical properties of such granular systems under a small enough stress deviator (before yielding).

One motivation of the present work is the study of highly concentrated non-Brownian suspensions (Péclet number  $\text{Pe} = +\infty$ ), modeled as assemblies of nearly touching grains bonded by a viscous lubricant [73, 74, 75]. Ideal lubrication effectively suppresses the tangent forces. Lubricated dynamics has already been employed as a means to obtain the force-carrying contact network of frictionless rigid particles, as the set of viscous bonds on which stresses concentrate [65]. Although crude, our current model should be able to reproduce the behavior of dense suspensions in the quasistatic limit. In this régime, the system evolves *via* a sequence of equilibrium states. At some point, the initial network is no longer able to sustain the imposed stress, it becomes unstable and a dynamic “crisis” occurs. Consequently, the evolution of the system is not quasistatic in the strictest sense (each point of the configuration space cannot be reached through a continuous series of equilibrium configurations). However, details of the dynamic are expected to be irrelevant. Thus we expect that the same equilibrium states will be visited in the quasistatic limit by both frictionless granular systems and dense suspensions with frictional grains. According to the simple toy model of Sec. III E 3, a dense suspension might be sketched by a slider moving on a bumpy surface in a media of viscosity  $\eta$ . Close to the quasistatic limit, the most important parameter would be the dimensionless number  $\eta\dot{\gamma}/P$ . One may notice that it is very similar to the parameter  $I_v$  introduced by Cassar *et al.* that controls submarine avalanches in what they call the viscous regime [76]. Steady shear simulations evidenced that the material is still able to flow with a volume fraction approximately equal to  $\Phi^* = \Phi_{\text{RCP}} \simeq 0.64$ . This result is consistent with theoretical results pertaining to suspensions, where the volume fraction  $\Phi^*$  at which the viscosity of the suspension diverges is believed to tally with the random close packing volume fraction [77]. However, it is not in agreement with the experiments exposed in [6], where the value of  $\Phi^*$  was found to be below 0.61. This discrepancy very likely originates in small scale features

of the experimental system that are not accounted for a model of perfectly lubricated spherical beads. The behavior of dense suspensions is known to be strongly impacted by short-range physics [78]. In the near future, we plan to study lubricated pastes with frictional contacts in the spirit of the simplified Stokesian dynamics scheme proposed by Ball and Melrose [73, 74, 75].

## APPENDIX A: DYNAMICAL EQUATIONS

In all three procedures O, D or S, at least one diagonal component of the stress tensor is imposed, while the conjugate cell dimension fluctuates. To perform such stress controlled computations, we resort to the Parrinello-Rahman method [32, 79, 80], with the same implementation as in Ref. [23], which can be consulted for more details. The position vector  $\mathbf{r}_i$  of particle  $i$  (defined with respect to an arbitrary origin), is rescaled to  $\mathbf{s}_i$ :

$$\mathbf{s}_i \equiv \underline{\underline{\mathbf{L}}}^{-1} \mathbf{r}_i \quad \text{for } 1 \leq i \leq N \quad (\text{A1})$$

with

$$\underline{\underline{\mathbf{L}}} = \text{diag}(L_1, L_2, L_3) \quad (\text{A2})$$

$\underline{\underline{\mathbf{L}}}^{-1}$  transforms the rectangular parallelipipedic simulation cell into a cubic box of unit edge length. The scaled position vector  $\mathbf{s}_i$  encodes the coordinates of the particle  $i$  in this mathematically defined box. It follows from Eq. A1 that the velocity  $\mathbf{v}_i$  of particle  $i$  is

$$\mathbf{v}_i = \underline{\underline{\mathbf{L}}}\dot{\mathbf{s}}_i + \dot{\underline{\underline{\mathbf{L}}}}\mathbf{s}_i \quad \text{for } 1 \leq i \leq N \quad (\text{A3})$$

Newtonian equations of motion for the scaled position vectors are written in the standard fashion ( $m_i$  denotes the mass of bead  $i$  and  $\mathbf{F}_i$  the overall force applied on particle  $i$  by its contacting neighbors):

$$m_i \ddot{\mathbf{s}}_i = \underline{\underline{\mathbf{L}}}^{-1} \mathbf{F}_i \quad \text{for } 1 \leq i \leq N \quad (\text{A4})$$

The time evolution of  $3N$  degrees of freedom is captured in Eq. A4. Like in [23], we discard some other terms present in the original, Hamiltonian Parrinello-Rahman (PR) scheme in (A4), since they are irrelevant at low strain rates in dissipative systems. Variables  $(L_\alpha)_{1 \leq \alpha \leq 3}$ , are either maintained constant, or satisfy an evolution equation derived from the PR method, as follows.

$$\begin{aligned} M \ddot{L}_\alpha &= \frac{1}{L_\alpha} \left[ L_\alpha^2 \sum_{i=1}^N m_i (\dot{s}_i^{(\alpha)})^2 + \sum_{1 \leq i < j \leq N} F_{ij}^{(\alpha)} r_{ij}^{(\alpha)} \right] \\ &\quad - \frac{\Omega}{L_\alpha} \Sigma_\alpha \quad \text{if } \sigma_\alpha \text{ is set to } \Sigma_\alpha \end{aligned} \quad (\text{A5})$$

$M$ , in (A5), is a generalized mass parameter,  $\mathbf{r}_{ij}$  is the vector joining the center of bead  $i$  to that of bead  $j$ , with the appropriate nearest image convention. The dynamical equations introduce an additional parameter, mass

	Procedure O	Procedure D	Procedure S
$(\mathbf{s}_i)_{1 \leq i \leq N}$	Eq. A4	Eq. A4	Eq. A4
$L_1$	Eq. A5	constant	Eq. A5
$L_2$	Eq. A5	Eq. A5	Eq. A5
$L_3$	Eq. A5	constant	Eq. A5
$\dot{\gamma}$	0	constant	Eq. A6
Direction 1	PBC	PBC	PBC
Direction 2	PBC	LE	LE
Direction 3	PBC	PBC	PBC

TABLE X: First part of the table: equation used for cell size and strain in procedures O, D and S. Second part of the table: boundary conditions employed in procedures O, D and S (PBC stands for periodic boundary condition and LE for Lees-Edwards boundary condition).

$M$  in Eqs. (A5) and (A6). In our simulations it was set equal to the sum of masses of all particles in the system. All changes in measured quantities such as friction coefficient, density or the fluctuations thereof on dividing  $M$  by 1000 were checked to be negligible, throughout the range of  $I$  values investigated.

The quantity within square brackets in Eq. A5 is  $\Omega \sigma_{\alpha\alpha}$ , with the Cauchy stress tensor as in Eq. (5). Thus Eq. (A5) will cause the cell to expand in direction  $\alpha$  if the current stress level is higher than the prescribed value  $\Sigma_\alpha$  and to shrink if it is smaller.

The last degree of freedom is the shear strain rate  $\dot{\gamma}$ . The Lees-Edwards (LE) boundary condition means that the conditions for periodicity in direction 2 and the definition of nearest images have to be redefined, as sketched on Fig. 1.  $\dot{\gamma}$  is equal to zero in procedure O, it is constant in procedure D, and varies in procedure S, until equilibrium is reached with  $\sigma_{12} = \tau$ . In this latter case one has:

$$\begin{aligned} M L_1 \dot{\gamma} &= \frac{1}{L_2} \left[ L_1 L_2 \sum_{i=1}^N m_i \dot{s}_i^1 \dot{s}_i^2 + \sum_{1 \leq i < j \leq N} F_{ij}^2 r_{ij}^1 \right] \\ &\quad - \frac{\Omega}{L_2} \Sigma_{12} \quad \text{if } \sigma_{12} \text{ is constrained to } \tau \end{aligned} \quad (\text{A6})$$

Eq. A6 is adapted from Eq. A5, and ensures  $\sigma_{12} = \tau$  in equilibrium or, on average, in a steady state flow. Note that with our sign convention, both  $\dot{\gamma}$  and  $\tau$  are negative in the situation depicted on Fig. 1.

Equations A4, A5 and A6, or the alternative condition on the corresponding strain parameter completely determine the dynamics of the system. Relevant equations and boundary conditions employed for each simulation procedure are summed up in Table X. Second-order equations A4, A5 and A6 are solved numerically by an order-three Gear predictor-corrector scheme [32].



## APPENDIX B: FABRIC TENSOR AND EXPANSION IN SPHERICAL HARMONICS

The density of contact normal directions,  $E(\theta, \varphi)$ , defined on the unit sphere  $\mathbb{S}^2$ , can be expanded on the Hilbertian basis of spherical harmonics  $Y_l^m$ :

$$E(\theta, \varphi) = \sum_{l=0}^{+\infty} \sum_{m=-l}^l c_{l,m} Y_l^m(\theta, \varphi), \quad (\text{B1})$$

with:

$$c_{l,m} = \iint_{\mathbb{S}^2} \overline{Y_l^m(\theta, \varphi)} E(\theta, \varphi) d\Omega. \quad (\text{B2})$$

$E$  satisfies  $E(\theta, \varphi) = E(\pi - \theta, \varphi + \pi)$  (parity symmetry) since the intergranular contacts are not oriented. This symmetry implies  $c_{l,m} = 0$  for  $l$  odd.

Even order fabric tensors encode coefficients  $c_{l,m}$ . We restricted ourselves to the fabric tensor of order 2,  $\underline{\mathbf{F}} = \langle \vec{n} \otimes \vec{n} \rangle$ .  $\underline{\mathbf{F}}$  yields the decomposition of  $E$  as a combination of spherical harmonics  $Y_l^m$  with  $l \leq 2$ .

If  $(Y_2^m)_{-2 \leq m \leq 2}$  are expressed with Cartesian coordinates, as

$$\begin{aligned} Y_2^{\pm 2}(x_1, x_2, x_3) &= \sqrt{\frac{15}{32\pi}} \frac{x_1^2 - x_2^2 \pm 2ix_1x_2}{r^2} \\ Y_2^{\pm 1}(x_1, x_2, x_3) &= \mp \sqrt{\frac{15}{8\pi}} \frac{x_1x_3 \pm ix_2x_3}{r^2} \\ Y_2^0(x_1, x_2, x_3) &= \sqrt{\frac{5}{16\pi}} \frac{3x_3^2 - r^2}{r^2}, \end{aligned}$$

one obtains from (B2):

$$\begin{aligned} c_{2,-2} + c_{2,2} &= 2\sqrt{\frac{15}{32\pi}} (F_{11} - F_{22}) \\ c_{2,-2} - c_{2,2} &= 2\sqrt{\frac{15}{32\pi}} 2iF_{12} \\ c_{2,-1} + c_{2,1} &= 2\sqrt{\frac{15}{8\pi}} iF_{23} \\ c_{2,-1} - c_{2,1} &= 2\sqrt{\frac{15}{8\pi}} F_{13} \\ c_{2,0} &= \sqrt{\frac{5}{16\pi}} (3F_{33} - 1) \end{aligned}$$

At order 2:

$$\begin{aligned} E(\theta, \varphi) &= \frac{1}{4\pi} + c_{2,0} Y_2^0(\theta, \varphi) \\ &+ c_{2,2} Y_2^2(\theta, \varphi) + \overline{c_{2,-2} Y_2^{-2}(\theta, \varphi)} \\ &+ c_{2,1} Y_2^1(\theta, \varphi) + \overline{c_{2,-1} Y_2^{-1}(\theta, \varphi)}. \quad (\text{B3}) \end{aligned}$$

since  $\overline{Y_l^m(\theta, \varphi)} = (-1)^m Y_l^{-m}(\theta, \varphi)$  (a well known property of spherical harmonics), and  $E$  takes real values. Finally, one has

$$\begin{aligned} E(\theta, \varphi) &= \frac{1}{4\pi} + c_{2,0} Y_2^0(\theta, \varphi) \\ &+ 2\Re(c_{2,2} Y_2^2(\theta, \varphi)) + 2\Re(c_{2,1} Y_2^1(\theta, \varphi)) \quad (\text{B4}) \end{aligned}$$

from which Eq. 28 follows on setting:

$$\begin{aligned} d_{xy}(\theta, \varphi) &= \frac{15}{8\pi} \sin^2 \theta \sin(2\varphi) \\ d_{x^2-y^2}(\theta, \varphi) &= \frac{15}{16\pi} \sin^2 \theta \cos(2\varphi) \\ d_{z^2}(\theta, \varphi) &= \frac{15}{16\pi} (3 \cos^2 \theta - 1) \\ d_{xz}(\theta, \varphi) &= \frac{15}{4\pi} \sin \theta \cos \theta \cos \varphi \\ d_{yz}(\theta, \varphi) &= \frac{15}{4\pi} \sin \theta \cos \theta \sin \varphi. \end{aligned}$$

## APPENDIX C: CRYSTALLIZATION UNDER SHEAR

Small samples, in both D and S-type simulations, tend to form strongly ordered structures under shear. This phenomenon, which did not occur for  $N > 1000$ , is briefly reported here. A more detailed study would be outside the scope of the present paper, and would require some investigation of the role of cell shape and boundary conditions, which is necessarily important in such small systems.

2 out of 3 S-type samples with  $N = 256$  and stiffness level  $\kappa_2$ , and 2 out of 2 D-type samples with  $N = 500$ ,  $I = 3.2 \times 10^{-4}$  and  $\kappa = \kappa_1$  present the following anomalies. First, solid fractions are considerably higher than  $\Phi_{\text{RCP}}$  (and even more so considering the size effect [21, 23] on  $\Phi$ ), with values approximatively equal to 0.67 (see fourth line of Tab. IV). Apparent friction coefficients are also particularly large. A lower bound for the static macroscopic friction coefficient of S-type ordered samples is 0.4, whereas dynamic macroscopic friction coefficient  $\mu^*$  of D-type ordered samples for  $I = 3.2 \times 10^{-4}$ ,  $\kappa = \kappa_1$ , and  $N = 500$  may overshoot by 20% the corresponding friction coefficient in bigger samples that do not experience any ordering. S-type samples also have very large coordination numbers,  $8 \leq z \leq 9$ . This latter characteristic is a clear indicator of partial crystalline order, as one necessarily has  $z \leq 6$  in generically disordered situations. The denser crystal arrangements, face-centered cubic (fcc) and hexagonal compact (hcp) (and stacking variants thereof), have  $z = 12$ .

For steady shear-rate-controlled D simulations, anomalous values of  $\Phi$  and  $\sigma_{12}$  appear after strains of order 5.

In order to detect crystalline order more quantitatively, we use the standard order parameters  $Q_6$  and  $Q_4$  employed in [23, 56, 81, 82]. First, all neighboring pairs of particles for which the center to center distance is smaller than  $1.4a$  are declared to be joined by a *bond* (this distance is approximately the first minimum of pair correlation function  $g(r)$  [23]). Then, local order parameters  $Q_i$  are associated to each grain  $i$ , as:

$$Q_i^{\text{loc}}(i) = \left[ \frac{4\pi}{2l+1} \sum_{m=-l}^{m=l} |\hat{q}_{lm}(i)|^2 \right]^{1/2}, \quad (\text{C1})$$

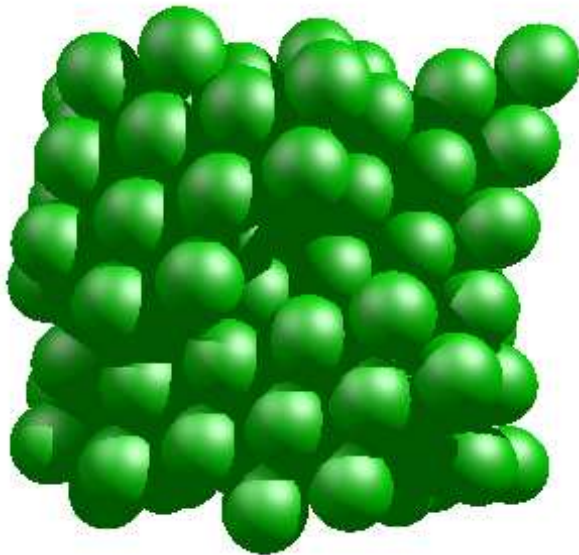


FIG. 18: Crystalline order induced by shear in one S sample with  $N = 256$ .

in which  $\hat{q}_{lm}(i)$  is an average over all neighbors  $j$  of  $i$  numbered from 1 to  $N_b(i)$ , the number of bonds of  $i$ :

$$\hat{q}_{lm}(i) = \frac{1}{N_b(i)} \sum_{j=1}^{N_b(i)} Y_{lm}(\mathbf{n}_{ij}), \quad (\text{C2})$$

$\mathbf{n}_{ij}$  denoting the unit vector pointing from the center of  $i$  to the center of  $j$ .

First, values of the pair  $(Q_4, Q_6)$  can be used to distinguish different local environments. In [23], following [56], the frequency of occurrence of ranges of values  $(0.191 \pm 0.05, 0.574 \pm 0.05)$  and  $(0.097 \pm 0.05, 0.485 \pm 0.05)$ , respectively corresponding to fcc-like and hcp-like configurations around one grain, were recorded. In the present case, most samples had very similar proportions of hcp-like and fcc-like local arrangements as in the RCP states studied in [23]: about 12% of beads fall in the hcp category, and fcc-like ones are virtually absent. The exceptions are the samples with anomalous, crystal-like properties, for which, while none of the beads has an fcc-like environment in that sense, the proportion of the hcp-like category raises to about 60% in S samples and to 40% in D ones.

A direct visualization, Fig. 18, reveals strikingly ordered configurations. A tentative conclusion to those preliminary observations is that the small samples tend to crystallize on somewhat shear-distorted hcp lattices.

One convenient characterization of order that is not sensitive to the distortion of crystalline patterns was suggested in [81], and used in [23] (those references may be consulted for the details that are not reproduced here). It amounts to extracting, by a suitable normalization, the “direction” of  $(\hat{q}_{6m}(i))_{-6 \leq m \leq 6}$  (an element of the unit sphere in a 13-dimensional space) and then using the correlations of such “angular” parts of local order parameters to identify “crystalline” bonds, and “crystalline” clusters of grains. With this method, more than 90% of the particles of the anomalous samples are declared to belong to crystalline regions.

- 
- [1] H. J. Herrmann, J.-P. Hovi, and S. Luding, eds., *Physics of Dry Granular Media* (Balkema, Dordrecht, 1998).
- [2] H. Hinrichsen and D. E. Wolf, eds., *The Physics of Granular Media* (Wiley-VCH, Berlin, 2004).
- [3] R. García Rojo, H. J. Herrmann, and S. McNamara, eds., *Powders and Grains 2005* (Balkema, Leiden, 2005).
- [4] A. Castellanos, *Advances in Physics* **54**, 263 (2005).
- [5] J. J. Stickel and R. L. Powell, *Annu. Rev. Fluid Mech.* **37**, 129 (2005).
- [6] G. Ovarlez, F. Bertrand, and S. Rodts, *Journal of Rheology* **50**, 259 (2006).
- [7] J. F. Brady, *Journal of Chemical Physics* **99**, 567 (1993).
- [8] D. Cumberland and R. Crawford, *The Packing of Particles* (Elsevier, Amsterdam, 1987).
- [9] O. Reynolds, *Philosophical Magazine* (5th series) pp. 469–481 (1885).
- [10] D. M. Wood, *Soil Behaviour and Critical State Soil Mechanics* (Cambridge University Press, 1990).
- [11] P. W. Rowe, *Proceedings of the Royal Society of London* **A269**, 501 (1962).
- [12] P. A. Cundall and O. D. L. Strack, *Géotechnique* **29**, 47 (1979).
- [13] J.-N. Roux and F. Chevoir, *Bulletin des Laboratoires des Ponts et Chaussées* **254**, 109 (2005).
- [14] J. F. Brady and G. Bossis, *Annual Review of Fluid Mechanics* **20**, 111 (1988).
- [15] F. da Cruz, S. Emam, M. Prochnow, J.-N. Roux, and F. Chevoir, *Phys. Rev. E* **72**, 021309 (2005).
- [16] T. Hatano, *Physical Review E* **75**, 060301(R) (2007).
- [17] A. Taboada, N. Estrada, and F. Radjaï, *Physical Review Letters* **97**, 098302 (2006).
- [18] C. Thornton, *Géotechnique* **50**, 43 (2000).
- [19] A. S. J. Suiker and N. A. Fleck, *ASME Journal of Applied Mechanics* **71**, 350 (2004).
- [20] D. Bideau and A. Hansen, eds., *Disorder and Granular Media* (Elsevier, 1993).
- [21] C. O’Hern, L. E. Silbert, A. J. Liu, and S. R. Nagel, *Physical Review E* **68**, 011306 (2003).
- [22] A. Donev, S. Torquato, and F. H. Stillinger, *Phys. Rev. E* **71**, 011105 (2005).
- [23] I. Agnolin and J.-N. Roux, *Phys. Rev. E* **76**, 061302 (2007).
- [24] G. Combe and J.-N. Roux, *Physical Review Letters* **85**, 3628 (2000).
- [25] J.-N. Roux and G. Combe, *C. R. Académie des Sciences (Physique)* **3**, 131 (2002).
- [26] A. V. Tkachenko and T. A. Witten, *Physical Review E* **62**, 2510 (2000).
- [27] J. D. Goddard and A. K. Didwania, *Quarterly Journal of Mechanics and Applied Mathematics* **51**, 15 (1998).

- [28] L. E. Silbert, D. Ertas, G. S. Grest, T. C. Halsey, and D. Levine, *Physical Review E* **65**, 031304 (2002).
- [29] N. Xu and C. S. O'Hern, *Physical Review E* **73**, 061303 (2006).
- [30] K. L. Johnson, *Contact Mechanics* (Cambridge University Press, 1985).
- [31] E. Somfai, J.-N. Roux, J. Snoeijer, M. van Hecke, and W. van Saarloos, *Phys. Rev. E* **72**, 021301 (2005).
- [32] M. Allen and D. Tildesley, *Computer simulations of liquids* (Oxford University Press, Oxford, 1987).
- [33] R. J. Bathurst and L. Rothenburg, *Mechanics of Materials* **9**, 65 (1990).
- [34] J. Christoffersen, M. M. Mehrabadi, and S. Nemat-Nasser, *Journal of Applied Mechanics* **48**, 339 (1981).
- [35] J.-P. Hansen and I. R. McDonald, *Theory of Simple Liquids* (Academic Press, 1986).
- [36] P. Rognon, J.-N. Roux, D. Wolf, M. Naaïm, and F. Chevoir, *Europhysics Letters* **74**, 644 (2006).
- [37] F. Da Cruz, F. Chevoir, D. Bonn, and P. Coussot, *Phys. Rev. E* **66**, 051305 (2002).
- [38] GDR MiDi, *European Physical Journal E* **14**, 341 (2004).
- [39] P. Jop, Y. Forterre, and O. Pouliquen, *Nature* **44**, 727 (2006).
- [40] I. Agnolin and J.-N. Roux, *Phys. Rev. E* **76**, 061303 (2007).
- [41] I. Agnolin and J.-N. Roux, *Phys. Rev. E* **76**, 061304 (2007).
- [42] E. Aharonov and D. Sparks, *Phys. Rev. E* **65**, 051302 (2002).
- [43] F. Radjaï and S. Roux, in [2], pp. 165–187.
- [44] H. Flyvbjerg and H. Petersen, *Journal of Chemical Physics* **91**, 461 (1989).
- [45] L. Rothenburg and N. P. Kruyt, *International Journal of Solids and Structures* **41**, 5763 (2004).
- [46] N. P. Kruyt and L. Rothenburg, *Journal of Statistical Mechanics; Theory and Experiment* p. P07021 (2006).
- [47] L. Oger, S. Savage, D. Corriveau, and M. Sayed, *Mechanics of Materials* **27**, 189 (1998).
- [48] L. Quartier, B. Andreotti, S. Douady, and A. Daerr, *Physical Review E* **62**, 8299 (2000).
- [49] F. Radjaï, M. Jean, J.-J. Moreau, and S. Roux, *Phys. Rev. Lett.* **77**, 274 (1996).
- [50] D. L. Blair, N. W. Mueggenburg, A. H. Marshall, H. Jaeger, and S. R. Nagel, *Physical Review E* **63**, 041304 (2001).
- [51] F. Radjaï, H. Troadec, and S. Roux, in *Granular Materials: Fundamentals and Applications*, edited by S. J. Antony, W. Hoyle, and Y. Ding (Royal Society of Chemistry, Cambridge, 2004), pp. 157–183.
- [52] L. E. Silbert, A. J. Liu, and S. R. Nagel, *Physical Review E* **73**, 041304 (2006).
- [53] H. A. Makse, N. Gland, D. L. Johnson, and L. Schwartz, *Physical Review E* **70**, 061302 (2004).
- [54] F. Calvetti, G. Combe, and J. Lanier, *Mechanics of Cohesive-frictional materials* **2**, 121 (1997).
- [55] M. M. Kohonen, D. Geromichalos, M. Scheel, C. Schier, and S. Herminghaus, *Physica A* **39**, 7 (2004).
- [56] T. Aste, M. Saadatfar, and T. J. Senden, *Phys. Rev. E* **71** (2005).
- [57] J.-N. Roux, *Physical Review E* **61**, 6802 (2000).
- [58] A. Donev, R. Connelly, F. H. Stillinger, and S. Torquato, *Phys. Rev. E* **75**, 051304 (2007).
- [59] E. Aharonov and D. Sparks, *Phys. Rev. E* **60**, 6890 (1999).
- [60] S. Ouaguenouni and J.-N. Roux, *Europhysics Letters*, **39**, 117 (1997).
- [61] F. Radjaï, D. E. Wolf, M. Jean, and J.-J. Moreau, *Physical Review Letters* **80**, 61 (1998).
- [62] S. N. Coppersmith, C. H. Liu, S. Majumdar, O. Narayan, and T. A. Witten, *Physical Review E* **53**, 4673 (1996).
- [63] L. E. Silbert, G. S. Grest, and J. W. Landry, *Physical Review E* **66**, 061303 (2002).
- [64] W. H. Press, B. P. Flannery, S. A. Teukolsky, and W. T. Vetterling, *Numerical Recipes* (Cambridge University Press, 1988).
- [65] S. Ouaguenouni and J.-N. Roux, *Europhys. Lett.* **32**, 449 (1995).
- [66] C. Brito and M. Wyart, *Europhysics Letters* **76**, 149 (2006).
- [67] P.-E. Peyneau and J.-N. Roux (2008), in preparation.
- [68] E. Azéma, F. Radjaï, R. Peyroux, and G. Saussine, *Phys. Rev. E* **76** (2007).
- [69] F. Varnik, L. Bocquet, J.-L. Barrat, and L. Berthier, *Phys. Rev. Lett.* **90** (2003).
- [70] F. Varnik, L. Bocquet, and J.-L. Barrat, *J. Chem. Phys.* **120** (2004).
- [71] O. Pouliquen, *Phys. Fluids* **11**, 542 (1999).
- [72] A. Daerr and S. Douady, *Nature* **399**, 241 (1999).
- [73] J. Melrose and R. Ball, *Europhys. Lett.* **32**, 535 (1995).
- [74] J. Melrose and R. Ball, *J. Rheol.* **48**, 961 (2004).
- [75] R. Ball and J. Melrose, *Physica A* **247**, 444 (1997).
- [76] C. Cassar, M. Nicolas, and O. Pouliquen, *Phys. Fluids* **17** (2005).
- [77] A. Sierou and J. Brady, *J. Fluid Mech.* **448**, 115 (2001).
- [78] J. Melrose and R. Ball, *J. Rheol.* **48**, 937 (2004).
- [79] M. Parrinello and A. Rahman, *Journal of Applied Physics* **52**, 7182 (1981).
- [80] M. Parrinello and A. Rahman, *Journal of Chemical Physics* **76**, 2662 (1982).
- [81] I. Volkov, M. Cieplak, J. Koplik, and J. R. Banavar, *Physical Review E* **66**, 061401 (2002).
- [82] V. Luchnikov, A. Gervois, P. Richard, L. Oger, and J.-P. Troadec, *Journal of Molecular Liquids* **96-97**, 185 (2002).